Title
Mesoporous Block Copolymer Battery Separators

Author
Wong, David Tunmin

Publication Date
2012

Peer reviewed|Thesis/dissertation

Mesoporous Block Copolymer Battery Separators

by

David Tunmin Wong

A dissertation submitted in partial satisfaction of the

requirements for the degree of

Doctor of Philosophy

in

Chemical Engineering

in the

GRADUATE DIVISION

of the

UNIVERSITY OF CALIFORNIA, BERKELEY

Committee in charge:

Professor Nitash P. Balsara, Chair

Professor John S. Newman

Professor Daryl C. Chrzan

Fall 2012

Abstract

Mesoporous Block Copolymer Battery Separators

by

David Tunmin Wong

Doctor of Philosophy in Chemical Engineering

University of California, Berkeley

Professor Nitash P. Balsara, Chair

In the past two decades, lithium-ion batteries have emerged as an increasingly important technology. They are used almost ubiquitously in laptops and cell phones because of their relatively high energy densities when compared to other battery chemistries. More recently, lithium-ion batteries have been employed in the automotive sector in both pure electric vehicles and hybrid electric vehicles. However, one of the major barriers in the widespread adoption of lithium-ion batteries in electric vehicles is the relatively high cost of these batteries. Despite being an inactive component, the battery separator has the highest specific cost of any component in the battery. Battery separators are typically composed of high molecular weight polyolefins (ie. polyethylene, polypropylene) that are made porous in one of two ways. The pores are made by either stretching the films uniaxially to make holes, in the so-called dry method, or by blending with another low molecular weight polyolefin that is extracted later to make holes, in the so-called wet method.[1-3] Neither of these methods produces holes in an equilibrium fashion. Whereas the cost of raw polypropylene is ~1-2 \$ kg^{-1}, the cost of battery separators is ~120-240 \$ kg^{-1}.[4] This large increase in cost is due primarily to the aforementioned manufacturing and quality control steps. In this thesis, we discuss the use of self-assembling block copolymers to synthesize mesoporous battery separators, which offer the potential to greatly reduce the cost of battery separators.

Our approach for synthesizing mesoporous battery separators utilizes the ability of block copolymers to self-assemble into well-defined morphologies. We blend a polystyrene-*block*-polyethylene-*block*-polystyrene (SES) copolymer with homopolymer polystyrene (PS) and then solvent cast nonporous films of these blends. We use a homopolymer selective solvent to remove the homopolymer PS, leaving a mesoporous film. There are several important considerations in this design. The PE block of the copolymer is semi-crystalline, which allows for the retention of a non-collapsing pore phase after homopolymer extraction. Ideally, the homopolymer PS segregates preferentially to the PS phase of the SES copolymer during the blending step. The ability of the homopolymer PS to segregate to this phase is largely dictated by the size of the

homopolymer PS (N_{PS}) relative to the size of the PS chains in the SES copolymer ($N_{PS,BCP}$). We define the parameter α as equal to this ratio: $\alpha = N_{PS} / N_{PS,BCP}$. We found that intermediate values of α , between 0.2 and 0.5, allowed the homopolymer PS to reside primarily within the PS domain, thus taking advantage of block copolymer self-assembly and enabling the formation of a continuous porous phase after homopolymer extraction. The morphological characterization of these mesoporous block copolymer films is non-trivial, and we employ a variety of techniques to study them.

This thesis is organized into 5 chapters. Chapter 1 describes the synthesis and preparation of the mesoporous block copolymer membranes, in addition to some of the characterization techniques used in this thesis. In Chapter 2, we discuss the relationship between the conductivity (in a liquid electrolyte) and morphology of the SES separators. We focus on the importance of α on the overall porosity of the structure. As traditional block-copolymer characterizations techniques proved inadequate to properly describe the morphology, in Chapter 3, we discuss the use of resonant soft x-ray scattering (RSoXS) to fully characterize the mesoporous block copolymer films. By tuning the incident x-ray energy, we were able to contrast match the three phases of our system (voids, polystyrene, and polyethylene). In Chapter 4, we study the impact of the washing step on the final film properties. Normally, the SES/PS cast films are immersed first in tetrahydrofuran (THF) to remove the homopolymer PS, and then in methanol (MeOH). Both THF and MeOH are nonsolvents for crystalline PE, but THF is a good solvent for both amorphous PE and PS, whereas MeOH is a poor solvent for all phases. Despite the fact that films were exposed to both THF and MeOH, the final solvent treatment (THF or MeOH) has a dramatic effect on both the conductivity and morphology of the film. In Chapter 5, we study the effect of changing the length of the PE block of the SES copolymer while maintaining the length of the PS block. We also benchmark our SES separators using tensile strength experiments and as full cell batteries against a commercial battery separator.

Table of Contents

Lists of Figures

List of Tables

List of Symbols

A	Electrode area, mm^2
A_0	Initial cross-sectional area of film for tensile strength measurements, mm^2
C	Fitting parameter for Equation 3
$C_{i,j}$	X-ray scattering contrast between two phases, i and j, where i and j can be PS, PE, or void
a_m	Area per molecule of a monolayer, 0.162 nm^2 for N_2
a_s	Specific surface area, m^2/g
$a_{s,P}$	A of the polymer/void interface per unit volume determined from Porod's law, m^{-1}
Δb	X-ray scattering length density difference, nm^{-2}
d_{BC}	Domain size of primary scattering peak of SES copolymer from SAXS, nm
d_{280eV}	Domain size of primary scattering peak for porous SES films from RSoXS at E = 280 eV, nm
$d_{284.2eV}$	Domain size of primary scattering peak for porous SES films from RSoXS at E = 284.2 eV, nm
d_{SAXS}	Domain size of primary scattering peak for porous SES films from SAXS, nm
$d_{SAXS,UW}$	Domain size of primary scattering peak for unwashed SES films from SAXS, nm
d_{SEM}	Domain size of primary scattering peak for porous SES films from SEM, nm
E	X-ray energy, eV
E	Young's modulus, MPa
F	Axial force, N.
h	Planck's Constant, 4.136 x 10^{-15} eV s
I	Azimuthally averaged scattering intensity, a.u.
$I_{abs,cal,GC}$	Scattering intensity of calibrated glassy carbon provided with the standard, cm^{-1}
I_{Cor}	Azimuthally averaged scattering intensity for samples measured with our instrumentation and corrected using Equation 4, a.u.
$I_{cor,GC}$	Azimuthally averaged scattering intensity for glassy carbon measured with our instrumentation and corrected using Equation 4, a.u.
I_{raw}	Azimuthally averaged scattering intensity for samples measured with our instrumentation without any corrections, a.u.
I_{RSoXS}	Azimuthally averaged scattering intensity determined by RSOXS, a.u.
I_{SAXS}	Azimuthally averaged scattering intensity SAXS and normalized using Equations 4 and 5, cm^{-1}
k	Boltzmann constant
l	Porous SES film thickness swollen with electrolyte, mm

L	Avogadro's number
m	Mass of the absorbent (BET calculations), g
m_{dry}	Mass of dry separator film, g
m_{swollen}	Mass of swollen separator film, g
n	X-ray scattering index of refraction
n_{m}^{a}	Monolayer capacity, see Equation 3
N	Number of monomers units normalized by the monomer volumes using a reference volume of 0.1 nm^3
N_h	Number of PS homopolymer monomer units normalized by the monomer volumes using a reference volume of 0.1 nm^3
$N_{mon,i}$	Number of chemical repeat units of PE (C4 units) or PS
p	Equilibrium pressure, Pa
p^{o}	Saturation pressure, Pa
q	X-ray scattering vector, nm^{-1}
q^*	X-ray scattering vector, nm^{-1}
R_{b}	Bulk resistance determined from AC impedance experiments, Ω
S	Stress, N mm^{-2}
S_{YS}	Yield stress, N mm^{-2}
t	Thickness of x-ray scattering samples, mm
T	Sample transmission normalized by the empty cell
T	Absolute temperature, K
v_i	Monomer volume for i (PS or PE)
v_{ref}	Reference volume, 0.1 nm^3
Δx	Axial displacement, mm.
x_0	Initial gauge length, mm.

Greek

α	Ratio of the molecular weight of the PS homopolymer to that of the PS in the block copolymer
β	Imaginary component of index of refraction
δ	Real component of index of refraction
η	Scaling factor for glassy carbon, see Equation 6
ε	Strain, $\Delta x / x_0$
θ	Scattering angle, rad
λ	X-ray wavelength, nm
ρ_{elec}	Density of electrolyte, g cm^{-3}
ρ_{mem}	Density of the porous polymer membrane, g cm^{-3}
ρ_{poly}	Density of SES copolymer, g cm^{-3}
σ	Conductivity, mS cm^{-1}

ϕ_{Elec}	Relative volume fraction of electrolyte in swollen SES copolymer
$\phi_{\text{PE,BCP}}$	Volume fraction of PE in SES copolymer
$\phi_{\text{PS,BCP}}$	Volume fraction of PS in SES copolymer
ϕ_{V}	Void fraction in SES copolymer film
$\chi_{PE\,/\,PS}$	Flory-Huggins interaction parameter between PE and PS

Acknowledgements

During my five and a half years at Berkeley, I have had the privilege of getting to know a lot of great people. Many of these people have provided invaluable insight into my research project, while others have simply been good friends.

I would to first thank my family. Both of my parents have supported me in more ways than I can properly thank them for. They have never wavered in their belief in me, and I am grateful for that. My brother, Kevin, who despite living on the opposite side of the country has often been the first person I have shared important news with, both good and bad. Through it all, he has always kept my best interests at heart. My cousins CT, Vicki, and Salim, who all lived nearby in the south bay, took care of me like I was a younger brother: feeding me and playing video games with me. With the rest of my immediate family scattered across the east coast, I always felt at home at Vicki and Salim's house.

My labmates have become my extended family here. Shrayesh Patel, who has been in the same research group as me since our days at Georgia Tech, was always available to lend an ear or offer his hand to help. Dr. Keith Beers was always ready with both a joke and a scientific discussion, depending on what the situation called for. Dr. Scott Mullin always had an overly elaborate engineering solution for every problem and a sense of humor about how ridiculous it was. Dr. Greg Stone did a great job at keeping everything in perspective and was always willing to share his experience. Dr. Nisita Wanakule and Dr. Alisyn Nedoma were both always willing and excited to talk about science or anything else that I had questions about. Alex Teran and Nick Young were available with crazy ideas both related and unrelated to research. The younger students, Kevin Wujcik, Jacob Thelen, Katherine Harry, and Chae-Young Shin have been fun to work with, and their enthusiasm has made the past several month more enjoyable. Our group has had a lot of great post-docs work here, and I wanted to acknowledge a few of them that I had the opportunity to work with closely: Dr. Daniel Hallinan, Dr. Liang Chen, Dr. Chelsea Chen, and Dr. Sebnem Inceoglu.

The college of chemistry at Berkeley has been staffed with several helpful and friendly people. The chemical engineering graduate office has continually been staffed by great people: Aileen Harris, Rocio Sanchez, Fred Deakin, Alegria Garcia, and Carlet Altamirano. Jim Breen has fixed the vacuum line for me more times than I am willing to admit. Eric Granlund helped me design and build a lot of things that were indispensable for my research.

Outside of lab, I have had a lot of friends to help me maintain my sanity in grad school. I leave the Isothermal PBRs as repeat college of chemistry summer softball champions. Our intramural ultimate frisbee and basketball teams both played well and were a lot of fun to play on. Both Cal Ultimate and Cal Racquetball are made up of a great group of people, and I will miss the practices, pickup games, and tournaments. I want to also acknowledge a lot of other good

friends that fall outside of those groups: Dr. Hannah Ray, Leah Faw, Tina Chiu, Kevin Wang, Monica Liou, Dr. Jordan Rosefigura, Craig Dana, Dr. Ting-Ying Chung, Nathan Craig, and Alan Berger.

At LBL and the ALS, I had the privilege of working with a lot of good scientists. Dr. Cheng Wang, Dr. Anthony Young, and Dr. Jeff Kortright helped guide me in RSoXS experiments, which much of my thesis is about. Dr. Alex Hexemer, Dr. Eric Schaible, Dr. John Pople, and Steven Alvarez were invaluable to SAXS experiments. Dr. Bernd Gludovatz helped me with tensile strength experiments. Dr. Vince Battaglia, Dr. Wei Zhang, and Xiangyun Song helped me with battery experiments.

I want to thank my thesis committee and qualifying exam committees for taking the time to listen to my ideas and provide feedback on my research. Prof. Newman, Prof. Chrzan, Prof. Segalman, and Prof. Graves all helped guide me through my research project.

As with any manuscript, I will list my advisor, Prof. Nitash Balsara at the end, even in my acknowledgements. This is not to undercut his importance to the process, but rather to emphasize that everything goes through him. He has been an excellent research advisor to me, and I am thankful for all of his helpful insight. I am still amazed at how quickly he can motivate me with his enthusiasm for science.

This work was supported by the Assistant Secretary for Energy Efficiency and Renewable Energy, Office of Vehicle Technologies of the U.S. Department of Energy under Contract No. DE-AC02-05CH11231 under the Batteries for Advanced Transportation Technologies (BATT) Program.

Chapter 1 – Synthesis and Characterization Techniques

1.1 Introduction

This thesis is focused primarily on the synthesis and characterization of mesoporous block copolymers and our experiments testing these materials as battery separators. Our approach is to blend polystyrene-*block*-polyethylene-*block*-polystyrene (SES) copolymers with polystyrene homopolymer (PS) and cast films of these blends. The nonporous films were then washed using a homopolymer selective solvent to remove the PS homopolymer, leaving a mesoporous film. In the blending step, the PS homopolymer goes to the PS phase of the SES copolymer, leaving a polyethylene (PE) matrix with pores lined with PS. We select SES as our copolymer for mesoporous films because the PE block is semi-crystalline, which allows for the formation of non-collapsing pore domains, and the PS block gels in the presence of our liquid electrolyte, increasing electrolyte retention and conductivity.[5] Triblock copolymer SES was used instead of the diblock copolymer SE because of the enhanced material properties of triblock copolymers.[6, 7] In this chapter, we focus on the synthesis and characterization techniques used in this thesis. In the subsequent chapters where the experimental methods are different, we specify those changes in the individual chapters.

1.2 Synthesis and characterization of block copolymers

Polystyrene-*block*-polybutadiene (SB) copolymers were synthesized by sequential anionic polymerization using *sec*-butyl lithium as the initiator.[8] The initiated chains were coupled using dibromoethane to produce symmetric SBS triblock copolymers.[9] The use of a nonpolar solvent (cyclohexane) results in polybutadiene chains with approximately 93% 1,4-addition. SBS was saturated using *p*-toluenesulfonyl hydrazide (p-TSH) in the presence of equimolar tri-*n*-propyl amine (TPA).[10] The reaction scheme is shown in Figure 1. Homopolymer PS was also synthesized by anionic polymerization using *sec*-butyl lithium as the initiator. The melt densities used for PE and PS are 0.78 and 0.97 g cm^{-3}, respectively, at 140 ^{o}C.[11] The molecular weight of the PS block of the SBS copolymer were obtained by extracting an aliquot of the reaction mixture during synthesis prior to butadiene addition. The PS molecular weight was measured on a Viscotek GPC Max VE-2001 equipped with a TDA 302 triple-detector system calibrated using PS standards with tetrahydrofuran (THF) as the eluent. The volume fractions of each block of the SBS copolymer and the ratio of 1-2 versus 1-4 vinyl addition in the polybutadiene (PB) blocks of each copolymer were determined using ^{1}H nuclear magnetic resonance (NMR) spectroscopy ($CDCl_3$, 25 ^{o}C). High temperature NMR (toluene-d_8, 90 ^{o}C) was used to ensure the complete saturation of the vinyl groups in the polybutadiene block of the SES copolymer. The polydispersity indices of the homopolymers were less than 1.06. The coupling reactions used to synthesize the triblock were not perfect, typically resulting in approximately 75% triblock and 25% diblock. The polydispersity indices of the two populations of chains were less than 1.05. We report the polymers used in each chapter in their respective experimental sections.

To remove saturation reagents, SES copolymers were precipitated drop-wise in methanol, redissolved in *o*-xylene at 100 °C, and then washed in a separatory funnel with excess deionized water. This procedure was repeated three times. The polymer was then dried under vacuum at 80 °C for 2 days. PS homopolymers were purified by precipitation in methanol. The homopolymers were then redissolved in benzene and precipitated two more times, filtered through a 0.2 µm filter, and freeze-dried in a lyophilizer (Millrock LD85).

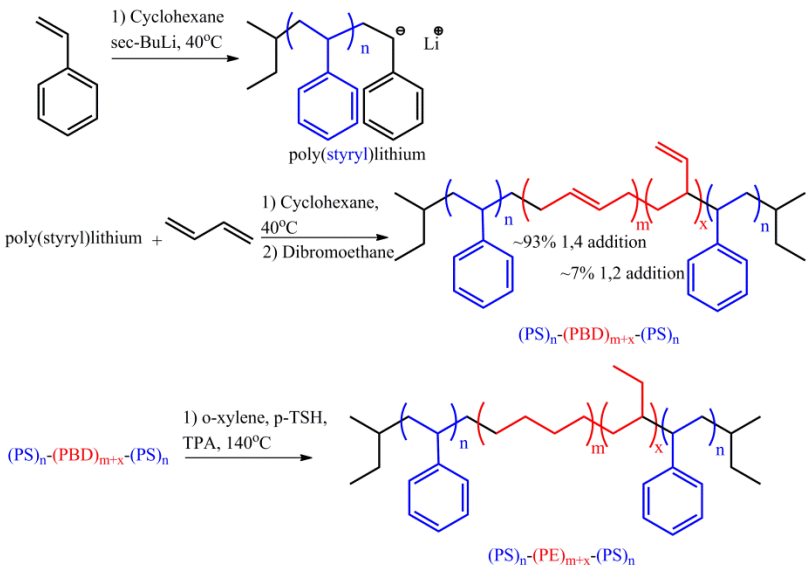

Figure 1. SES copolymer synthesis schematic.

1.3 Film preparation

Films of SES/PS blends were prepared using a custom-built solvent caster consisting of a doctor blade to control film thickness and a heated stage to control film temperature (see Figure 2). The top surface of the solvent caster consists of a porous aluminum vacuum plate, upon which fresh sheets of aluminum foil are applied to create pristine substrates. Solutions of SES, PS, and *o*-xylene were prepared at 120 °C and doctor-bladed onto aluminum foil at 80 °C. The smoothness and thickness of the films depended mainly on the SES concentration, and 0.05 g SES per mL *o*-xylene was used to create the films. After drying the film on the caster for 15 minutes at 80 °C, the films were further dried at 25 °C in a vacuum oven for 4 hours. The dried, nonporous SES/PS films were immersed in tetrahydrofuran (THF) to dissolve out the PS homopolymer chains. This was followed by immersion in methanol (MeOH). Each immersion step lasted for 1-2 min and the films were wet when they were transferred from one solvent to the other. Typically, after 2 immersions in each solvent, the films could be separated from the aluminum foil with ease. The final solvent washing step for most of the films in this thesis is MeOH. In Chapter 4, we discuss the effect of THF as the final solvent washing step. Films were then dried in a vacuum oven for 4 hours at 25 °C to produce the porous separators. In all cases,

the difference in mass of the films, measured before and after the THF/MeOH-washing and subsequent drying steps, was within experimental error of the mass of homopolymer PS added in the first step (± 2%). We thus define the nominal void fraction, ϕ_V, as the fraction of volume occupied by the PS homopolymer in the SES/PS mixture prior to dissolution. ϕ_V is calculated from the composition of the films and densities of PE, PS, and SES at 140 ^oC. Our estimate of ϕ_V does not account for changes in volume due to crystallization of PE, vitrification of PS, or changes in the pore geometry that may arise during cooling. We define α as the ratio of the molecular weight of the PS homopolymer to that of the PS in the block copolymer (specified in each chapter). For the blends at any given ϕ_V, the same relative mass of PS homopolymer is added regardless of α .

The properties of the films thus produced are compared with a commercially available Celgard 2400 membrane, a polypropylene battery separator made using the dry process. We used two different batches of Celgard 2400. For the Celgard 2400 membrane produced in 2005, ϕ_V = 0.37, as specified by the manufacturer (Chapter 2). For the Celgard 2400 membrane produced in 2011, ϕ_V = 0.41 (Chapter 3,5).

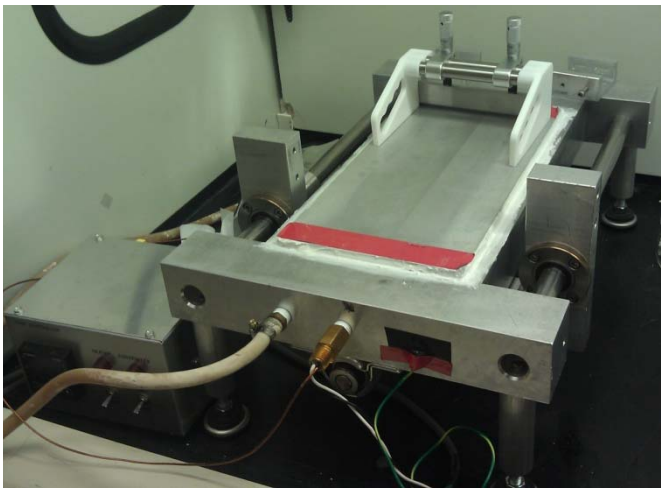

Figure 2. Custom-built solvent caster used to prepare SES films.

1.4 Ionic conductivity measurements

Conductivity measurements were performed using Swagelok cells with polished electrodes having a diameter of 22.2 mm. Polymer samples were cut out using a 22.2 mm diameter punch, weighed, and then placed into a standard lithium battery electrolyte solution of 1.0 M lithium hexafluorophosphate ($LiPF_6$) in ethylene carbonate/diethyl carbonate (1:1 v/v, Novolyte Technologies, Inc.) for at least 2 days. The swollen films were placed in the Swagelok cells and the impedance was measured using a potentiostat (Bio-Logic VMP3) over a frequency

range from 1 MHz to 500 mHz at a peak-to-peak amplitude voltage of 10 mV. Conductivity, σ, is calculated using the equation

$$\sigma = l/(AR_b), \quad (1)$$

where A is the electrode area, l is the measured sample thickness, and R_b is the bulk resistance determined from the intersection of the impedance data with the real axis on the Nyquist plot. For samples with higher resistance, the sample resistance was taken as the low frequency minimum of semi-circles obtained in the Nyquist plot. All conductivity measurements were taken at room temperature. The thickness of the samples, l, used in the conductivity calculations was measured using a micrometer after the impedance spectroscopy measurements were completed. This thickness was about 10% less than that of the dry electrolyte films due to effects such as plastic deformation under the applied stress in the conductivity cell. In Figure 3, we show a typical Nyquist impedance plot. In this plot, we take the intersection of the data with the real axis as R_b = 2.6 Ω, which can be converted to σ = 0.27 mS/cm, using A = 3.9 cm^2 and l = 0.0027 cm. Electrolyte uptake measurements were made by blotting electrolyte-swollen films and weighing them after conductivity and film thickness measurements. The volume fraction of electrolyte in the film, ϕ_E, was calculated from the known weights of the dry film and the electrolyte uptake, using the room temperature densities of the polymer [12] and the electrolyte (ρ_{elec} = 1.26 g cm^{-3}, ρ_{poly} is calculated for each block copolymer, and ρ_{poly} = 0.78 g cm^{-3} for Celgard® 2400), ignoring the possibility of non-ideal mixing between SES and the electrolyte. ϕ_E is $[(m_{swollen} - m_{dry})(1-\phi_V)]/[\rho_{elec}(m_{dry}/\rho_{poly})]$, where m_{dry} and $m_{swollen}$ are the dry and swollen weights of the film.

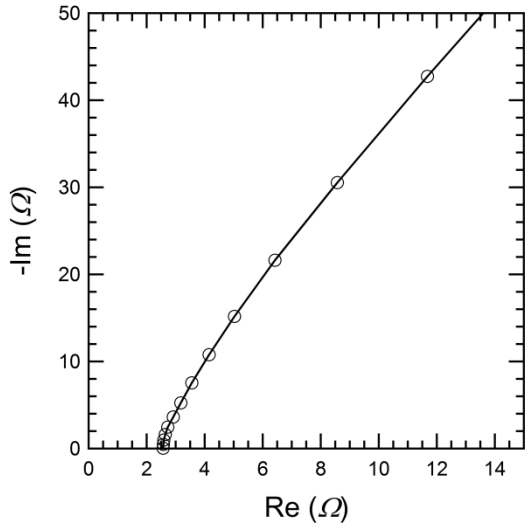

Figure 3. Typical Nyquist impedance plot.
The negative of the imaginary component of the impedance (-Im) is plotted as a function of the real component of the impendance (Re). R_b is taken as the intersection of the impedance data with the real axis, and conductivities are calculated using Equation 1.

1.5 Nitrogen physisorption experiments

Nitrogen physisorption experiments were performed using a Micromeritics TriStar II instrument. Polymer films were cut into strips and dried under vacuum for 4 hours prior to the measurements. The Brunauer-Emmett-Teller (BET) method was employed to calculate an internal surface area for the films.[13] The specific surface area, $a_s(\mathrm{BET})$ can be calculated using

$$a_s(\mathrm{BET}) = \frac{n_m^a L a_m}{m} \tag{2}$$

where L is Avogadro's number, a_m is the area per molecule of a monolayer, which is 0.162 nm^2 for N_2, m is the mass of the absorbent, and n_m^a is the monolayer capacity. The monolayer capacity was calculated by fitting data to the linear BET equation,

$$\frac{p}{n^a(p^o - p)} = \frac{1}{n_m^a C} + \frac{C-1}{n_m^a C}\frac{p}{p^o} \tag{3}$$

where p is the equilibrium pressure, p^o is the saturation pressure, C is a fitting parameter related to the enthalpy of adsorption, and n^a is the measured volume of nitrogen adsorbed. Parameters C and n_m^a were obtained by fitting the data obtained at low p/p^o values. Further interpretation of physisorption data was based on IUPAC recommendations.[14]

1.5 Scanning electron microscopy

Scanning electron microscopy (SEM) images were taken using a Hitachi S-5000 Scanning Electron Microscope. Cast films were submerged in water and then cryofractured in liquid nitrogen, loaded onto a brass stub using carbon tape, and sputter coated with Au/Pd before imaging.

1.6 Small angle x-ray scattering

Small angle x-ray scattering (SAXS) experiments were used to characterize the bulk morphology of the SES membranes. Measurements were performed on beam line 7.3.3 at the Advanced Light Source at Lawrence Berkeley National Laboratory and beam line 1-4 of the Stanford Synchrotron Radiation Laboratory. Samples were stacked to a thickness of approximately 100-300 μm to increase scattering volume. A silver behenate sample was used as a standard, and data were reduced using the Nika program for Igor Pro available from Jan Ilavsky at the Advanced Photon Source (APS).[15] The azimuthally averaged scattering intensity, I, is reported as a function of the scattering vector q ($q = 4\pi\sin(\theta/2)/\lambda$), where θ is the scattering angle and λ is the wavelength of the incident beam.

1.7 Resonant soft x-ray scattering

RSoXS experiments were performed at beam line 11.0.1.2 at the Advanced Light Source.[16] Films were prepared in the same way as previously described, with the exception that less concentrated solutions were used (twice as much *o*-xylene) in order to cast films with thicknesses of approximately 10 μm. Thin samples (relative to SAXS) are essential for RSoXS to minimize artifacts due to absorption. We have verified that the morphologies are the same by comparing the scattering in SAXS (10 keV) with scattering in RSoXS at energies well-above the carbon K-edge of 285 eV (1 keV). After solvent treatment to remove the homopolymer, the SES films were loaded into the RSoXS chamber as free-standing films. Samples were measured using energies between 275 and 290 eV at a sample-to-detector distance of approximately 80 mm. Data were analyzed using a modified version of the same Nika program used in SAXS experiments.[16] Data were normalized by subtracting out a dark image.

Chapter 2 – Relationship Between Morphology and Conductivity of Block-Copolymer Based Battery Separators

Abstract

Nanoporous battery separators were made by blending a polystyrene-*block*-polyethylene-*block*-polystyrene copolymer (SES) and polystyrene (PS) homopolymers, casting films of the blend, and selectively dissolving the homopolymer. The efficacy of the separators thus obtained was determined by measurement of the ionic conductivity of separators soaked in 1.0 M lithium hexafluorophosphate in ethylene carbonate/diethyl carbonate (1:1 v/v, Novolyte Technologies, Inc.), a standard lithium battery electrolyte. We focus on the effect of chain length of the sacrificial homopolymer on separator morphology and ion transport. In highly porous separators with a nominal pore volume fraction of 0.43, conductivity peaked at α = 0.22, where values as high as 0.39 mS cm^{-1} were achieved (α is the molecular weight of the PS homopolymer normalized by that of the PS block in the SES copolymer). Nitrogen adsorption experiments and scanning electron microscopy were used to determine the underpinnings of this observation. At α = 0.12, extremely small pores with low surface area are formed. Increasing α to 0.22 results in a film with well-connected nanoscale pores. A further increase in α to 2.02 results in films with micron-sized pores that are not effective for ion transport.

2.1 Introduction

Nanoporous separators used in lithium ion technology are presently of considerable interest in spite of the fact that they are an inactive component of the battery. In most cases, the separators are composed of inert semi-crystalline polyolefins such as polyethylene or polypropylene. A liquid electrolyte contained in the pores is responsible for ion transport in the battery. Although these polyolefin materials cost only about 1-2 \$ kg^{-1}, the cost of a typical battery separator is in the vicinity of 120-240 \$ kg^{-1}.[4] This large increase in price is mainly due to the complex and carefully controlled processing steps used to generate the porous structure within the separator.

There are two different approaches for generating pores in battery separators: wet processes and dry processes. In wet processes, a membrane comprising a phase-separated mixture of an amorphous and a semi-crystalline polyolefin is immersed in a solvent at room temperature. Semi-crystalline polyolefins are typically soluble at elevated temperatures in the vicinity of the melting temperature. During solvent treatment only the amorphous polyolefin is solvated and removed, thus leaving behind a porous semi-crystalline structure.[1-3] In addition, films made by wet processes are stretched either before or after extraction to increase porosity, resulting in slightly oriented pore structures. In dry processes, pores are produced entirely by

stretching semi-crystalline polyolefin films. Pores are generated because the deformation tends to be localized in the amorphous regions of the semi-crystalline polyolefins. The pores obtained by dry processes tend to be straight and oriented perpendicular to the plane of the film. Uniaxially oriented films produced from dry methods have high tensile strengths only in the stretching direction, while films produced using the wet method typically have high tensile strength in all directions. The balance of tensile strength is not necessarily advantageous as tensile strength is primarily important for roll-to-roll battery manufacturing wherein films are pulled along one axis only.[1] Separators made via dry processes exhibit significantly lower tortuosities than those made via wet processes. Typically, separators made by dry processes are better suited for high power density applications, while those made by wet processes are better suited for long battery life applications. This is because the straight pores in separators made from the dry process allow a more direct path for ions to travel (higher power density), while separators made through the wet process are more tortuous and can suppress dendritic lithium that may form on the graphite anode (longer life).[3] The uniformity of the resulting pore structures is crucial for battery performance. Non-uniform pore structures will lead to non-uniform current distributions during battery operation. Defects in the separator can lead to catastrophic failure of batteries.

In conventional wet processes, the extent of phase separation in the membrane prior to the pore formation step is determined entirely by non-equilibrium effects.[17-21] This is because phase-separated structures that are created by blending immiscible substances above their melting temperatures (e.g. oil and water) will continue to coarsen until the heavier phase settles to the bottom of the container. In the case of polymers, this process is extremely slow due to slow molecular motion,[22-24] and it is thus feasible to trap phase-separated structures with characteristic length scales ranging from nanometers to microns. However, small changes in the processing conditions can lead to large changes in the phase-separated morphology which, in turn, affects pore structure. Since driving forces for phase-separation in polymers depends crucially on the molecular weight of the components,[25, 26] small changes in the molecular weight distributions of the amorphous and semi-crystalline components can also result in alterations of the pore structure.[27-30] This is a significant problem because commercial approaches for synthesizing polyolefins often lead to very broad molecular weight distributions. In this chapter we describe a new wet process that utilizes blends of anionically synthesized model block copolymers and homopolymers with relatively narrow molecular weight distributions to address these problems.

The membranes studied in this paper are composed of a polystyrene-*block*-polyethylene-*block*-polystyrene (SES) copolymer. The driving forces that lead to the formation of periodic microphase-separated structures in block copolymers are well-established.[31-33] The immiscibility of polystyrene (PS) and polyethylene (PE) results in phase-separation, but the covalent bond between the PS and PE chains restricts the size of the phase-separated domains to molecular dimensions (typically 10-50 nm). The size of the domains is governed by chain length, whereas the geometry of the microphases (e.g. lamellar or cylindrical) is governed by the PS-to-PE ratio. Depending on the balance between thermodynamic and kinetic driving forces, the PE crystals can either be trapped within the microphases or break out of them: this was quantified by Register, Ryan, and coworkers.[34-41] In the first step of our process, a non-porous membrane is made by solvent-casting a mixture of SES and PS. In the simplest case, the PS homopolymer simply swells the PS microphase of the block copolymer. Selective dissolution of PS (which is amorphous) results in the formation of nanoscale pores in a polyethylene matrix. There are two

crucial differences between the present process and those formed in conventional wet processes. First, the phase-separated morphology that is the basis for the porous structure of the final membrane is at equilibrium, and thus strict control of processing conditions during the first film forming step is not essential. Second, the pores are naturally lined with PS chains because of the structure of the SES copolymer. Since PS is slightly more polar than PE, it may lead to more complete filling of the porous structure with the electrolyte, which is especially of concern for structures with small-diameter pores.[42, 43] Although the functioning separators in this work are comprised entirely of the SES copolymer, this paper focuses on the role of the sacrificial PS homopolymers. In particular, we show that choosing the correct molecular weight of the sacrificial PS homopolymer to blend with the SES copolymer is crucial for obtaining membranes with well-connected pore structures.

While the present study is primarily motivated by fundamental aspects of the relationship between morphology and ion transport, the membranes described herein may also be of practical interest. Material costs of PE-containing block copolymers are about an order of magnitude higher than those of PE homopolymers. However, the simplicity of the proposed processing steps has the potential to reduce the overall cost of the finished separators.

The proposed approach of creating nanoporous block copolymer films has been used by others for a wide range of applications ranging from water filtration to drug delivery.[44-48] Phillip et al. generated monolithic nanoporous materials by synthesizing poly(DL-lactide)-*block*-polydimethylsiloxane-*block*-polystyrene, shear aligning the polymer, and selectively etching out the lactide block.[44] They generated membranes with well-defined cylindrical pores with diameters of about 15 nm and found that gas flow through the membranes followed Knudsen diffusion, while liquid flow obeyed the well-established Hagen-Poiseuille equation. Uehara et al. created porous films by exposing polystyrene-*block*-polyethylene copolymer films to fuming nitric acid [45]. Nitric acid selectively etches the PS microphase, which enables control of the pore diameter by adjusting exposure time. This enabled a systematic study of the effect of pore size on the diffusion of glucose and albumin. Yang et al. obtained films by spin-coating blends of homopolymer poly(methyl methacrylate) (PMMA) and polystyrene-*block*-poly(methyl methacrylate).[46, 47] The PMMA homopolymer was selectively dissolved, leaving behind cylindrical pores with a diameter of 15 nm. The diameter of the holes was reduced by deposition of gold inside the holes. This enabled a systematic study of the effect of pore size on drug release. Zhou et al. made films comprising polyisoprene (PI), PS, and a polyisoprene-*block*-polystyrene copolymer.[48] The concentrations of the components were chosen so that a bicontinuous microemulsion morphology was obtained. Crosslinking the PI chains enabled selective dissolution of the PS homopolymer, leaving pores with average diameters of approximately 45 nm. By comparing the conductivity of the membrane swollen with an ionic liquid with that of the pure ionic liquid, Zhou et al. concluded that their membrane had a tortuosity factor of about 2.

2.2 Experimental

Most of the characterization techniques used in this chapter are described in Chapter 1.

Polymers used

The molecular weights of the PS and PE blocks for the SES copolymer were 15 and 82 kg mol^{-1}, respectively, and the PE volume fraction, $\phi_{PE,BCP}$, was 0.77 (in the melt state at 140 ^{o}C). The melt density of the SES is 0.83 g cm^{-3} at 140 ^{o}C.[11]

Error analysis

Most of the properties reported in this chapter are mean values based on measurements on four or five independent samples. The reported error bars represent the standard deviation of the measurements. We do not report error estimates in the BET analysis because only one experiment was run (sample quantity limitations).

2.3 Discussion

Structure and morphology characterization

In Figure 4a we plot the electrolyte volume fraction, ϕ_E, versus void volume fraction, ϕ_V, for films with selected values of α. Also included in Figure 4a are our data obtained from Celgard® 2400. The dashed line in Figure 4a, a line through the origin with slope = 1, represents the expectation that $\phi_E = \phi_V$. It is evident that in most cases, $\phi_E \approx \phi_V$ (within experimental error). This implies that the nominal pore volume generated by our process is filled with electrolyte, regardless of void fraction and homopolymer chain length. The electrolyte uptake of our separators is similar to that of Celgard® 2400 when void fraction is matched. Regardless of α, ϕ_E increases with increasing ϕ_V. The only significant exception is at α = 0.12 and ϕ_V = 0.43, where ϕ_E is significantly lower than expected. In most cases, the data in Figure 4a lie slightly above the $\phi_E = \phi_V$ line. This is probably due to the elasticity of the separator. We plot ϕ_E as a function of α in Figure 4b at fixed ϕ_V of 0.35 and 0.43. We focus on this range of ϕ_V because current commercial separators have void volume fractions in this range. The lines in Figure 4b represent the expected value of ϕ_E for ϕ_V values of 0.35 and 0.43. It is clear that ϕ_E is a weak function of α when α exceeds 0.12. In other words, the amount of electrolyte in our films is not affected by the molecular weight of the sacrificial homopolymer above α = 0.12.

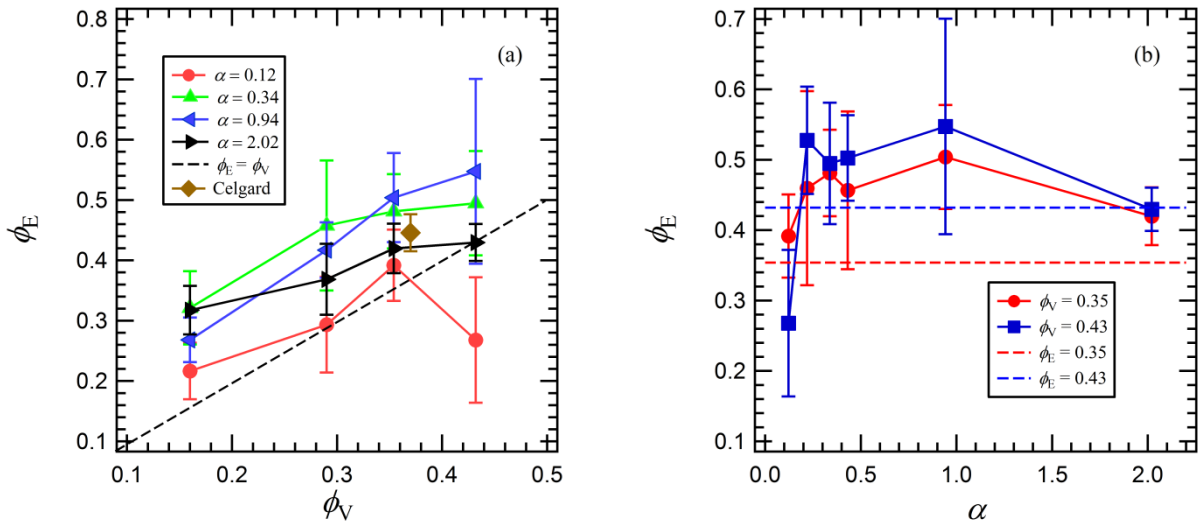

Figure 4. Electrolyte uptake for SES separators.
Electrolyte volume fraction in the separator, ϕ_E, as a function of a) void fraction, ϕ_V, for select values of the normalized chain length of the sacrificial homopolymer, α and b) α at $\phi_V = 0.35$ and 0.43. The dashed line in Figure 4a represents $\phi_E = \phi_V$. The dashed lines in Figure 4b represent $\phi_E = \phi_V = 0.35$ and $\phi_E = \phi_V = 0.43$.

Figure 5 shows typical results of nitrogen physisorption experiments, where the volume of nitrogen absorbed in the separator, n^a, is plotted as a function of relative pressure, p/p^o, during nitrogen adsorption and desorption. We show data for selected values of α at $\phi_V = 0.43$. The peak seen at high p/p^o in Figure 5 is expected in the case of slit-like pores. The hysteresis in adsorption and desorption indicates the presence of nanoscale pores. As α increases from 0.22 (Figure 5a) to 0.34 (Figure 5b), we see a significant increase in the amount of N_2 adsorbed, which indicates an increase in nanoporosity. Further increasing α to 0.94 results in a decrease in the amount of N_2 adsorbed. Finally, at $\alpha = 2.02$, we see very low amounts of nitrogen adsorption (Figure 5d), which suggests the presence of very few nanopores in the membranes. The data in Figure 5 indicate that the internal pore structure in our membranes at fixed ϕ_V is a sensitive function of α (similar data were obtained at other values of ϕ_V).

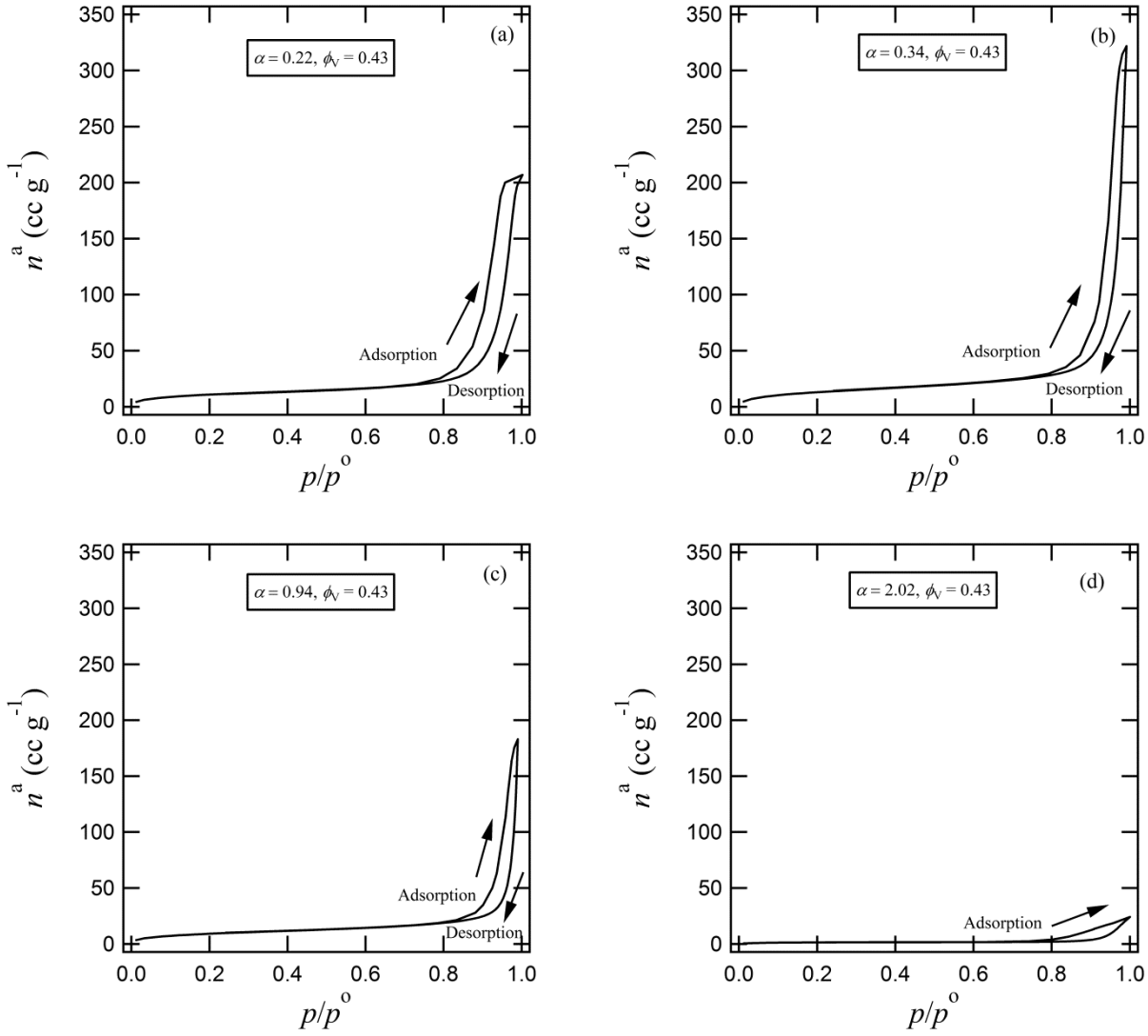

Figure 5. Results of N_2 physisorption experiments.
Plots of N_2 adsorbed as a function of p/p^o where p is the equilibrium pressure, and p^o is the saturation pressure at void fraction, ϕ_V = 0.43 for normalized chain lengths of the sacrificial homopolymer a) α = 0.22 b) α = 0.34 c) α = 0.94, and d) α = 2.02.

In Figure 6, the internal surface area, a_s(BET) , calculated using Equations 1 and 2, is plotted versus α for films with ϕ_V = 0.35 and 0.43 (same sample set is shown in Figure 4b). We find that a_s(BET) is peaked in the vicinity of α = 0.43 for both void fractions. These data indicate that separators with intermediate values of α have more accessible pores than those made with either very small values of α (e.g. 0.12) or very large values of α (e.g. 2.02).

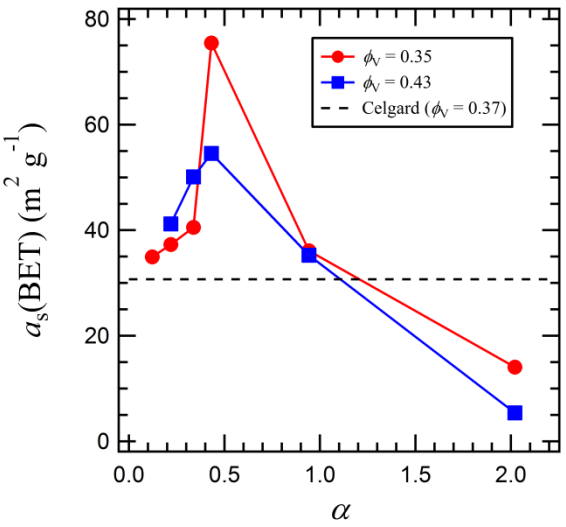

Figure 6. BET surface areas for SES separators.
Internal surface area measured by BET, a_s(BET) as a function of the normalized chain length of the sacrificial homopolymer, α, for select values of void fraction, ϕ_V, where the dashed line represents the a_s(BET) of Celgard® 2400.

Typical position-space images of the pore structure in our films, obtained by SEM, are presented in Figure 7, where micrographs obtained at ϕ_V = 0.43 are shown. The cross-sectional view in Figure 7a shows that α = 0.12 results in a very fine porous structure. Larger nanoscale pores can be seen in the film cross-sections at intermediate α values of 0.22 and 0.43 (Figure 7b and c). Figure 7d shows an interesting morphology of well-defined pores at α = 2.03, but the pore diameters are in the micron range. The SEM data thus confirm our earlier conclusion regarding the reduction in internal surface area in the α = 2.02, ϕ_V = 0.43 membrane.

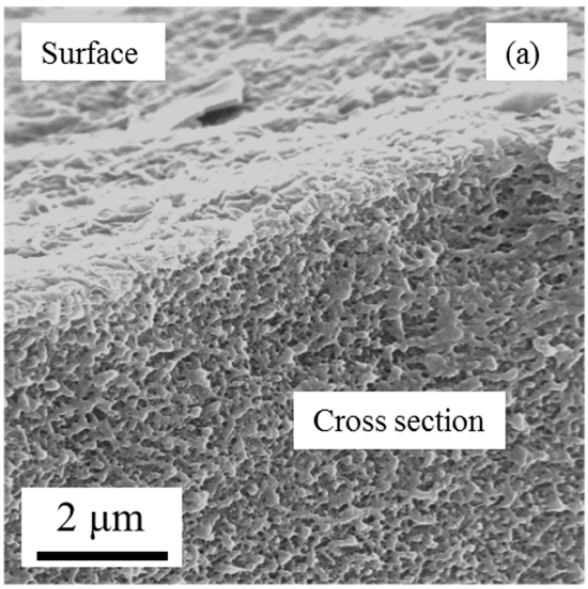

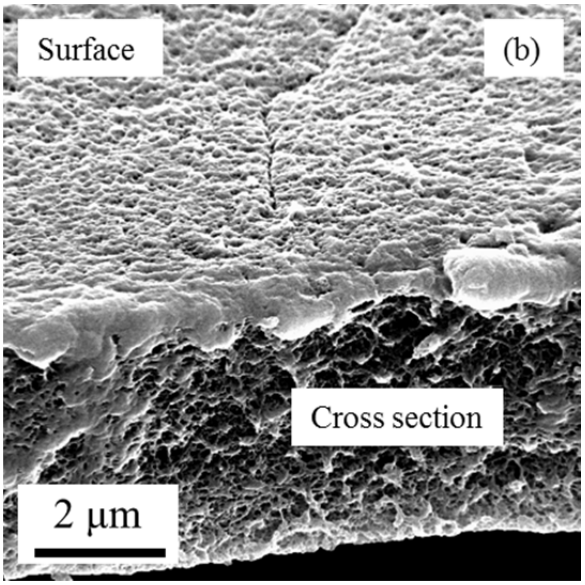

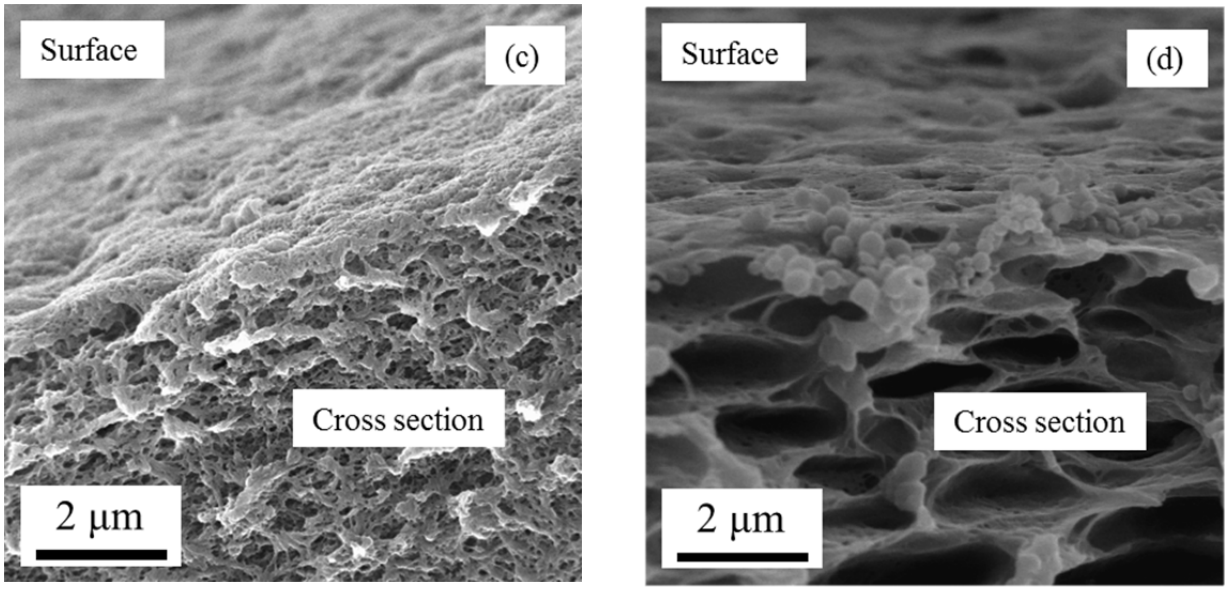

Figure 7. Scanning electron micrographs of SES separators.
Images are taken with void fraction, ϕ_V = 0.43 at a) α = 0.12, b) α = 0.22, c) α = 0.43, and d) α = 2.02 obtained by cryofracturing washed out films.

Ionic conductivity

In Figure 8a we plot ionic conductivity, σ, versus α for the ϕ_V = 0.43 membranes. Membrane conductivity peaks at α = 0.22 with a value of 0.39 mS cm^{-1}, which is comparable to that of Celgard® 2400. The conductivity peak in Figure 8a is highly asymmetric. It decreases precipitously when α decreases from 0.22 to 0.12. In contrast, the conductivity decreases gradually as α is increased from 0.22 to 2.02. Quite surprisingly, the ionic conductivity at α = 0.12 and 2.02 are similar. Another feature worth noting is that the size of the error bars for the ϕ_V = 0.43 membranes is relatively small. In Figure 8b, we plot σ versus α for the values of ϕ_V less than 0.43. At ϕ_V = 0.16, σ = 0.03 mS cm^{-1} regardless of the value of α. This value is considerably smaller than that obtained at ϕ_V = 0.43. It is likely that the pore structure is well connected at ϕ_V = 0.43 but poorly connected at ϕ_V = 0.16. Increasing ϕ_V to 0.29 and 0.35 results in an increase in σ, as seen in Figure 8b. There is, however, a concomitant increase in the error associated with the measurement of σ. The error bars decrease when ϕ_V is increased to 0.43. One explanation for the observed changes in the error bars is that it is difficult to obtain reproducible pore structures in the cross-over region between poorly connected (ϕ_V = 0.16, Figure 8b) and well-connected (ϕ_V = 0.43, Figure 8a) pores. The dashed lines in Figure 8b represent average values of σ for each of the ϕ_V values. The conductivity data are summarized in Figure 9, which shows the dependence of σ on ϕ_V and α. At ϕ_V = 0.16, 0.29, and 0.35, we show the average value of σ. In this range, we find the expected trend of increasing conductivity with increasing ϕ_V. At α = 0.22, this trend continues. Clearly, the α = 0.22, ϕ_V = 0.43 membrane exhibits the highest conductivity of the block copolymer separators obtained thus

far. This conductivity is comparable to that of Celgard® 2400, which is also shown in Figure 9. It is worth noting, however, that the Celgard membrane performance is more impressive because it has a lower void fraction than the optimized block copolymer membrane. This is, perhaps, not surprising, as the Celgard technology has been optimized for several years and is made using the dry process which leads to a reduction in tortuosity. In future work we will optimize the block copolymer-based separators and examine the possibility of outperforming current separators.

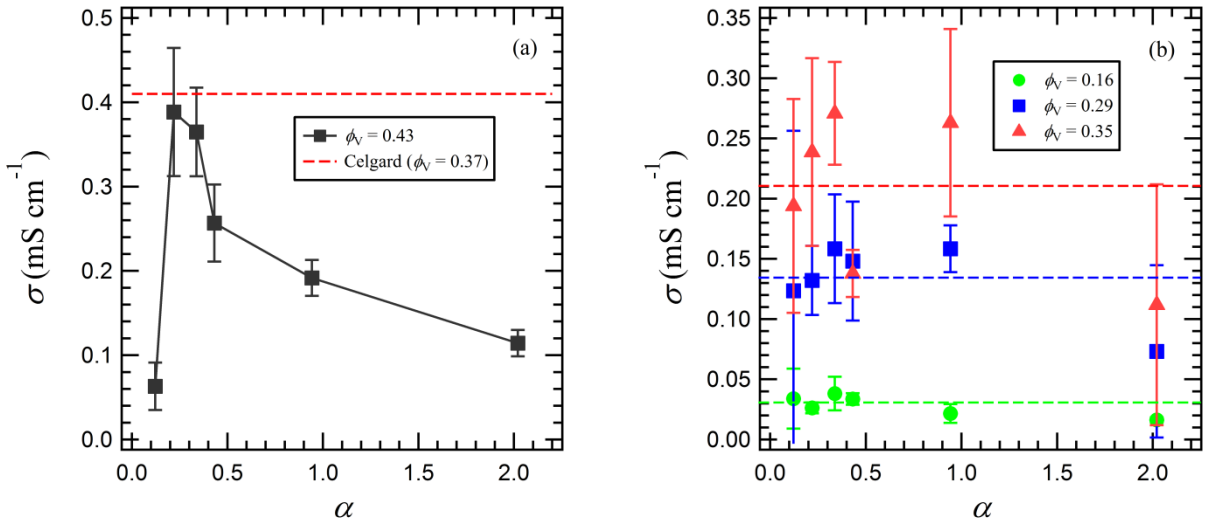

Figure 8. Ionic conductivity of SES separators as a function of α.
Ionic conductivity, σ, of SES separators soaked in 1.0 M $LiPF_6$/EC/DEC as a function of the normalized chain length of the sacrificial homopolymer, α for a) void fraction, ϕ_V = 0.43, where the dashed line represents the conductivity of Celgard® 2400 in the same electrolyte, shown for comparison, and b) ϕ_V of 0.16, 0.29, and 0.35, where the dashed lines represent the average σ of the corresponding ϕ_V.

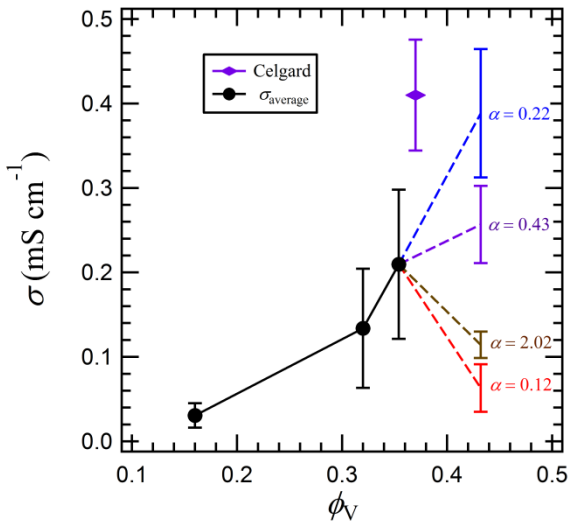

Figure 9. Ionic conductivity as a function of ϕ_V.
Ionic conductivity, σ, of SES separators soaked in 1.0 M $LiPF_6$/EC/DEC as a function of void fraction, ϕ_V, where σ at ϕ_V of 0.16, 0.29, and 0.35 is the average value across all values of α. σ at ϕ_V = 0.43 is plotted at α = 0.22, 0.43, 2.02, and 0.12.

Small angle x-ray scattering (SAXS)

The SAXS profile of pure SES copolymer at 140 ^oC, shown in Figure 10, exhibits a broad primary peak at $q = q^* = 0.14$ nm^{-1} and a shoulder at higher q values. The width of the primary peak indicates that the SES sample has relatively little long-range order. This may be a due to a combination of effects such as the complexity of the sample (an incompletely coupled triblock copolymer) and the processing steps used to create the sample. However, we expect the SES sample to contain hexagonally packed PS cylinders in a PE matrix, based on polystyrene-to-polyethylene volume fraction ratio of 0.23. The domain size of the morphology, $d = 2\pi / q^* =$ 45 nm. The higher order shoulder is attributed to a combination of the expected higher order peaks of the hexagonal phase at $q = \sqrt{3}q^*$ and $2q^*$. In contrast, SAXS data from SES/PS mixtures generally did not contain scattering peaks that could be easily interpreted in terms of morphology, particularly at the high values of ϕ_V that are of practical interest. In Figure 10, we show the scattering profiles of SES/PS blends with α = 0.22 and ϕ_V = 0.43 at 140 ^0C. The presence of a shoulder in the vicinity of $q = q^*$ suggests the presence of a characteristic length scale of about 45 nm. The absence of well-defined peaks indicates the lack of a simple periodic morphology. SAXS profiles obtained from the SES/PS blends with α = 0.22 and ϕ_V = 0.43 at 25 ^0C before and after washing, shown in Figure 10, also contain shoulders in the vicinity of $q = q^*$. However, these data are affected by the semicrystalline nature of the PE block in the SES copolymer, which can suppress the ordering of the block copolymer.[34-41] The length scale of the pores seen in the SEM data (Figure 7b) is outside the q-window available in SAXS. The SAXS data provide weak support for the presence of microphase separation of PE and PS domains on the 45 nm length scale.

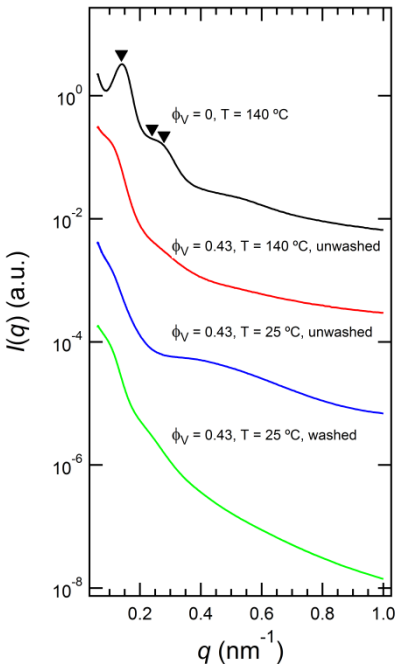

Figure 10. SAXS profile of SES copolymer and SES/PS copolymer blends before and after washing. The intensity, I, is plotted as a function of scattering vector, q. ϕ_V is used to represent the volume fraction of the PS homopolymer blended. The top profile represents the neat block copolymer. The annotations on the top profile represent the q^*, $\sqrt{3}q^*$, and $2q^*$ positions. The middle two profiles have homopolymer added, but the homopolymer has not been washed out. The bottom profile was taken after washing out homopolymer PS. The PS homopolymer for this blend is α = 0.22.

Discussion

The main observation of this study is that α, the normalized chain length of the sacrificial homopolymer, has a profound effect on membrane conductivity (Figure 8 and Figure 9). It is likely that this observation is a reflection of the morphology of the SES/PS film before the THF-washing step. However, based on very general arguments presented by Shull[49] and Leibler,[50] one expects the morphology of blends of A-B-A triblock copolymers and A homopolymers to depend on α. If $\alpha << 1$, then the A homopolymer is compatible with both A and B blocks and will thus be distributed uniformly in both blocks. Dissolving out the homopolymer in such a film will result in extremely small pores on the length scale of the A homopolymer (which is a very short chain) located in both A and B microdomains. On the other hand, if $\alpha >> 1$ then the homopolymer is expected to form separate macroscopic domains. Dissolving out the homopolymer in such a film will result in macroscopic pores. The localization of A homopolymer in the A microdomains of the block copolymer is only expected over an intermediate range of values of α. Dissolving out the homopolymer in such a film will result in nanoscale pores. This provides an explanation for the observed dependence of conductivity on α at ϕ_V = 0.43, reported in Figure 8a. At α = 0.12, the homopolymer chain length is too small, and it is distributed homogeneously in the PS-rich and PE-rich microphases. Thus, when the

homopolymer is extracted from this sample, a membrane with very small voids that are unrelated to the block copolymer morphology are formed (Figure 7a). In contrast, at α = 2.02, the homopolymer chain length is too large, and it macrophase-separates into micron-sized domains leading to the large pores seen in Figure 7d. One might anticipate that the pores in Figure 7d are more effective for transport than the small pores in Figure 7a. The transport measurements shown in Figure 8 and Figure 9 indicate otherwise. The porous structures shown in both Figure 7a and d are equally ineffective for transport. Nanoscale pores that are effective for transport are only seen at intermediates values of α, such as α = 0.22 (Figure 7b) and α = 0.43 (Figure 7c). The effect of morphology on transport is dramatic. At ϕ_V = 0.43, the ionic conductivity of the sample with α = 0.22 is 6 times greater that of the sample with α = 0.12. The a_s(BET) trends shown in Figure 6 are qualitatively similar to the conductivity trends reported in Figure 8a. The shapes of the curves in Figure 6 and Figure 8a are different; the former is peaked at α = 0.43, while the latter is peaked at α = 0.22. We do not have an explanation for these differences. It is clear that a complete understanding of the present system requires a study of the morphology of the polymer films before washing out the homopolymer. We address this issue in the following chapters.

2.4 Conclusions

Nanoporous battery separators were made by casting films of block copolymer/homopolymer blends and selectively removing the homopolymer. The volume occupied by homopolymer chains in cast films are thus converted into pores. This approach enabled systematic variation of the pore structure at fixed void fraction by changing the normalized chain length of the sacrificial homopolymer, α. The efficacy of the separators thus obtained was determined by measurement of the ionic conductivity of separators soaked in a standard liquid electrolyte. In highly porous separators with a fixed pore volume fraction of 0.43, conductivity was peaked at α = 0.22. Nitrogen adsorption and SEM were used to determine the underpinnings of this observation. At low values of α, conductivity is low because very small, poorly connected pores are formed. At high values of α, conductivity is low because very large pores are formed.

Chapter 3 – Mesoporous Block Copolymer Morphology Studied by Contrast Matched Resonant Soft X-Ray Scattering

Abstract

We demonstrate the use of contrast-matched resonant soft x-ray scattering (RSoXS) for studying the morphology of mesoporous polystyrene-*block*-polyethylene-*block*-polystyrene (SES) copolymer membranes. The mesoporous membranes were obtained by blending the SES copolymer and polystyrene (PS) homopolymer to obtain a non-porous membrane, followed by selective dissolution of the PS. If the PS homopolymer chains are initially located within the PS microphase of the SES copolymer, then one obtains a porous film wherein the pores are lined with PS. We refer to this as the templated morphology. The membranes are thus composed of three phases: voids, PS, and PE. Conventional techniques such as small angle x-ray scattering (SAXS) and scanning electron microscopy (SEM) distinguish only between the polymer and the voids. The main advance in this chapter is to show that microphase separation between PS and PE can be studied by contrast-matched RSoXS in spite of the presence of voids. Under certain circumstances, we obtain mesoporous membranes that are not templated by the SES copolymer. We show that RSoXS can be used to distinguish between templated and non-templated, mesoporous films.

3.1 Introduction

Mesoporous polymer membranes are used in a wide variety of applications including filtration, supports for gas separation membranes, and battery separators.[28, 46] The pores provide channels for transport while the solid polymeric phase gives structure to the membranes, providing them with mechanical and chemical properties necessary for manufacturing and using the membrane. It is often advantageous to generate pores that are lined with a different component than the structural component.[48, 51-56] For example, one might like to line the pores of water filtration membranes with a hydrophilic polymer. Clearly, the structural phase of this membrane must be hydrophobic. Block copolymers, which are chemically distinct polymers covalently bonded together, provide a convenient avenue for generating such mesoporous membranes.[48, 53, 55, 56] These membranes have three distinct phases: structural polymer, pore lining polymer, and voids. Traditional block copolymer characterization techniques, such as scanning electron microscopy (SEM) or small angle x-ray scattering (SAXS) [31, 57, 58] lack the capability to distinguish three phases. In both cases, the contrast between polymer and voids is much higher than that between the structural and pore-lining polymers. This precludes complete characterization of microphase separation in mesoporous polymer systems. Small angle neutron scattering (SANS) can be used to contrast-match phases, but this requires the incorporation of a varying amount of a deuterated polymer or solvent to amplify the difference in scattering length

density of different phases.[59, 60] Labeling polymer chains with deuterium can have a significant effect on the thermodynamic interactions between polymers.[61, 62] Interpretation of SANS data is predicated on quantification of these thermodynamic effects. In this work, we utilize resonant soft x-ray scattering (RSoXS) as a technique for generating contrast in multicomponent polymer systems.[63-68] Since contrast matching in RSoXS is obtained without labeling, interpretation of data does not require accounting for changes in thermodynamic interactions.

RSoXS has been used to study the morphology of several polymer systems. Mitchell and coworkers were able to distinguish the individual sizes for a blend of polyacrylate and polystyrene beads by using two different near-carbon K edge energies.[63] Virgili and coworkers demonstrated the utility of RSoXS for contrast enhancement of a thin film polystyrene-*block*-polyisoprene.[64] Wang and coworkers clearly defined the morphology of an ABC triblock copolymer, poly(1,4-isoprene)-*block*-polystyrene-*block*-poly(2-vinyl pyridine), as two nested hexagonally packed cylinder arrays, by comparing the position of the primary scattering peaks at multiple energies.[67] We use RSoXS to characterize the morphology of a mesoporous polystyrene-*block*-polyethylene-*block*-polystyrene (SES). In this paper, we demonstrate that microphase separation between the polystyrene (PS) and polyethylene (PE) blocks in the mesoporous films can be studied by tuning the energy of the incident X-rays in RSoXS experiments.

Mesoporous SES films were synthesized by blending the SES copolymer with polystyrene (PS) homopolymer, followed by selective solvent extraction of PS. Our procedure is described in Chapter 2 of this thesis.[69] These films were tested as battery separators, and it was found that the ionic conductivity of the resulting porous membranes in a liquid electrolyte depended strongly on the ratio of the molecular weight of the homopolymer polystyrene molecular weight to the block copolymer polystyrene molecular weight, which we define as α. It should be clear that pores lined with PS chains within a polyethylene (PE) structural phase are obtained only if the PS homopolymer is confined within the PS-rich microphase in the SES/PS blend prior to extraction. At a fixed ratio of SES/PS, the morphology of the SES/PS blend is dictated by the value of α. We study the SES membranes thus obtained as a function of α.

The purpose of this chapter is to determine the morphology of all of the phases of the membrane: the PE microphase, the PS microphase, and voids. Specifically, we address the issue of distortion of the equilibrium morphology of the neat block copolymer when it has been fashioned into a mesoporous membrane. While we focus on RSoXS results, we also present data obtained from a variety of standard characterization techniques including SAXS and SEM. We also present AC impedance spectroscopy on membranes soaked in an electrolyte. This chapter builds on an Chapter 2,[69] where we first described the synthesis and characterization of porous SES membranes.

3.2 Experimental

Most of the characterization techniques used in this chapter are described in Chapter 1.

Polymers used

The molecular weights of the PS and PE blocks for the SES copolymer were 13.5 and 67 kg mol^{-1}, respectively, and the PE volume fraction, $\phi_{PE,BCP}$, was 0.75 (in the melt state at 140 ^{o}C). The melt density of the SES is 0.83 g cm^{-3} at 140 ^{o}C [11].

Error analysis

The conductivity data reported are the average of at least 4-5 measurements. In the case of the x-ray scattering and SEM studies, experiments were repeated to verify results; we present only one set of data. Data from both techniques were used to determine characteristic length scales of the morphology of our system. The observed variance in the length scales determined was 2 nm.

3.3 Results and discussion

Samples

The samples discussed in this study are summarized in Table 1. The mesoporous membranes are distinguished by the value of α (ϕ_V is fixed at 0.43). For completeness, we include the neat SES sample without voids. The compositions of all of the samples in Table 1 are identical in that after homopolymer extraction, only the SES copolymer is left behind. The only difference is the geometry of the voids (or their absence). $\phi_{PE,BCP}$ and $\phi_{PS,BCP}$ are the volume fractions of PE and PS in the mesoporous films, respectively. ϕ_{Elec} is the volume fraction of electrolyte uptaken by the swollen film, and can be calculated by $(m_{swollen} - m_{dry})(1-\phi_V)/[\rho_{elec}(m_{dry}/\rho_{poly})]$, where m_{dry} and $m_{swollen}$ are the dry and swollen weights of the film, ρ_{elec} = 1.26 g cm^{-3}, is the density of the liquid electrolyte (1.0 M $LiPF_6$ in EC/DEC, 1:1 v/v), and ρ_{poly} = 0.83 g cm^{-3}, is the density of the SES copolymer in the melt state.

The thermodynamic properties of our system are governed by the Flory Huggins interaction parameter between PS and PE, $\chi_{PE/PS}$, and chain lengths. We estimate that the value of $\chi_{PE/PS}$ at 140 ^{o}C is 0.045 based on a reference volume, v_{ref}, of 0.1 nm^3.[70-72] The segregation between PS and PE blocks depends on $\chi_{PE/PS}N$, where N is the chain length of the block copolymer. We define N as the number of reference volume units per chain, $N = N_{mon,i}v_i / v_{ref}$, where $N_{mon,i}$ is the number of chemical repeat units of PE (C4 units) or PS, v_i is the monomer volume (0.179 nm^3 for PS and 0.119 nm^3 for PE), and v_{ref} is reference volume of 0.1 nm^3.[12, 70, 73] Thus N of the block copolymer is 1890, corresponding to $\chi_{PE/PS}N$ = 85. The pure block copolymer is thus in the strong segregation regime. For reasons that we

clarify below, we have calculated $\chi_{PE/PS}N_h$, where N_h is the homopolymer chain length based on v_{ref} and include these values in Table 1.

Table 1. All samples studied in this chapter.*

Sample	α	$M_{n,sacrificial,PS}$ (kg mol^{-1})	ϕ_V	$\phi_{PE,BCP}$	$\phi_{PS,BCP}$	ϕ_{Elec}	$\chi_{PE/PS}N_h$
Neat SES	-	-	0	0.755	0.245	-	-
Porous SES	0.13	1.7	0.43	0.43	0.14	0.35 ± 0.08	1.3
Porous SES	0.22	3.0	0.43	0.43	0.14	0.56 ± 0.06	2.3
Porous SES	0.36	4.8	0.43	0.43	0.14	0.54 ± 0.06	3.7
Porous SES	0.44	5.9	0.43	0.43	0.14	0.59 ± 0.05	4.6
Porous SES	0.90	12.2	0.43	0.43	0.14	0.46 ± 0.08	9.5
Porous SES	1.65	22.3	0.43	0.43	0.14	0.40 ± 0.02	17.3

*The normalized chain length of the sacrificial homopolymer, α, is calculated relative to the PS block of the SES copolymer, which is 13.5 kg mol^{-1}. Other variables listed in the table are: molecular weight of the sacrificial homopolymer PS, $M_{n,sacrificial,PS}$, void fraction of polymer films, ϕ_V, volume fraction of PE in the SES, $\phi_{PE,BCP}$, volume fraction of PS in the SES, $\phi_{PS,BCP}$, and volume fraction of electrolyte uptaken, ϕ_{Elec}. $\chi_{PE/PS}N_h$, is the product of the Flory-Huggins interaction parameter for PE/PS and homopolymer chain length based on v_{ref}.

Morphology of pure SES copolymer

In Figure 11, we show SAXS data for the neat SES block copolymer at 150 ^{o}C, which is well above the melting temperature of PE in our SES copolymer. We show the scattering profile above this temperature because the semi-crystalline nature of the PE block can distort the morphology of the block copolymer below the melting point.[35] In the melt, we can clearly distinguish the presence of two distinct peaks. The primary scattering peak for our block copolymer, $q^* = q_{BC}$ = 0.152 nm^{-1}. The presence of a clear q^* and $2q^*$ peak for a block copolymer with $\phi_{PS,BCP}$ = 0.245 indicates the presence of a hexagonal packed cylinder morphology.[74] The $\sqrt{3}q^*$ peak is absent because of a minimum in the form factor.[74] We define $d_{BC} = 2\pi/q_{BC} = 41.3$ nm.

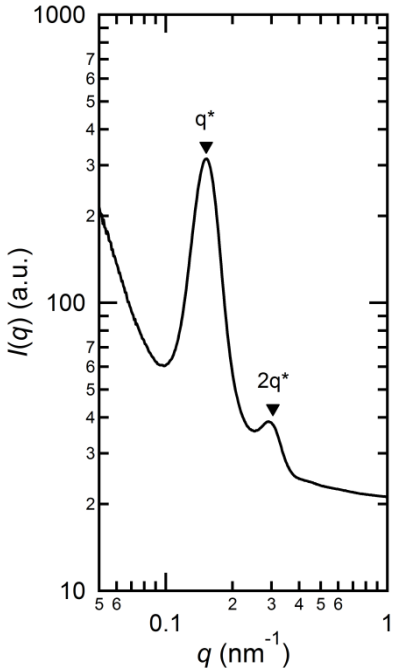

Figure 11. SAXS profiles for the neat SES block copolymer.
The intensity, $I(q)$, is plotted as a function of scattering vector, q (nm^{-1}). Data were collected at 150 °C. The scattering peaks q^* and $2q^*$ are indexed with inverted triangles.

Ionic conductivity of porous SES films

In Figure 12 we plot ionic conductivity, σ, versus α for the mesoporous samples listed in Table 1 after they were soaked in the electrolyte. The volume fraction of electrolyte taken up by the samples, ϕ_{Elec}, is given in Table 1. It is evident that ϕ_{Elec} is a weak function of α at a fixed void fraction, ϕ_V = 0.43. In contrast, σ is a sensitive function of α, with a maximum of 0.40 mS cm^{-1} at α values between 0.22 to 0.44. The σ of our porous separators approach the σ of our standard, Celgard® 2400, σ = 0.42 mS cm^{-1}. At low and high values of α, σ decreases rapidly. This dependence of σ on α is consistent with Chapter 2.[69]

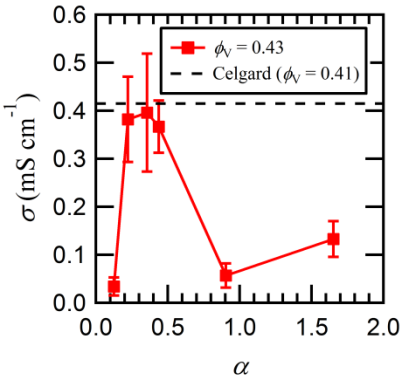

Figure 12. Ionic conductivity of SES separators.
Ionic conductivity, σ, of SES separators soaked in 1.0 M $LiPF_6$ in EC/DEC 1:1 v/v as a function of the normalized chain length of the sacrificial homopolymer, α. The dashed line represents the conductivity of Celgard® 2400 soaked in the same electrolyte.

SAXS and SEM of porous films

In Figure 13a-c, we show the expected dependence of the morphology of the unwashed SES/PS blend on α as described in our previous publication.[69] At small values of α, the homopolymer is miscible in both phases as shown in Figure 13a. We refer to this as the mixed case. Extracting the PS chains from such a blend will clearly not result in a mesoporous membrane templated by the block copolymer. We expect the homopolymer PS to penetrate the PE phase when the free energy penalty of placing a homopolymer chain in the PE phase when the energy is of the order kT, where k is the Boltzmann constant and T is absolute temperature, i.e. when $\chi_{PE/PS} N_h \approx 1$, or $N_h \approx 1/\chi_{PE/PS} = 22$, or $\alpha \approx 0.09$. At intermediate values of α (0.2-0.5), the PS homopolymer swells the PS-rich microphase. Extracting the PS chains from such a blend will result in PS-lined pores, as described in Figure 13b. We refer to this as the templated case. The main objective of this chapter is to characterize porous films obtained under these conditions. At large values of α, the PS chains exhibit macrophase separation as shown in Figure 13c. We refer to this as the macrophase separated case. Extracting PS chains from such a blend will result in macroporous membranes with poor pore connectivity. The scenarios described above ignore complications arising from structural relaxations that may occur during PS extraction and drying. It also assumes that the PE crystals are confined to the PE-rich microphases, i.e. no breakout crystallization.[34-36, 75, 76]

In Figure 13d, we show the surface SEM of the mesoporous membrane with α = 0.13. While pores on the 50-100 nm length scale are evident, their morphology is disordered and unrelated to typical morphologies obtained in microphase-separated block copolymer-homopolymer blends.[77-80] We take this as a signature of the mixed case (Figure 13a). The SEMs at α = 0.22 and 0.36 show slit-like pores in a lamellar morphology (Figure 13e and f). The pores are more clearly seen at α = 0.36. We take these SEMs as signatures of the templated case (Figure 13b). Quite surprisingly, increasing α to 0.96, results in a cylindrical morphology. The d-spacing and arrangement of the pores on a hexagonal lattice is consistent with SAXS data from the neat SES copolymer (Figure 11). A further increase of α to 1.65 results in a very rough surface with no discernible features on the mesoscale (Figure 13h). There is a notable

correspondence between the SEMS (Figure 13d-h) and the sketched morphologies (Figure 13a-c). Samples at α = 0.13 (Figure 13d), 0.36 (Figure 13f), and 1.65 (Figure 13h), compare well with schematics of the mixed, templated, and macrophase separated cases shown in Figure 13a, b, and c, respectively. The crossover from one regime to the next is smooth. The sample with α = 0.22 (Figure 13e) is located at the crossover from mixed to templated systems. The sample with α = 0.90 (Figure 13g) is located at the crossover from templated to macrophase separated systems. These SEM are limited, however, in that they provide information only on the surface morphology of these membranes. The cross-sections were also imaged using SEM by cryofracturing the porous films in water. These images were similar to those shown in Chapter 2. [69] and thus we do not present them in this chapter (see Figure 7).

SAXS is a standard approach for characterizing bulk morphologies of block copolymers.[81] In Figure 14a, we show SAXS data from the porous SES membranes at all values of α studied. Line-intensity profiles of the SEM micrographs shown in Figure 13 were used to determine the length scale of the periodic structure, d_{SEM}. The results of this exercise are represented in Figure 14a; the open circles in Figure 14a are located at $q = 2\pi / d_{SEM}$ (line scans of the SEMS of samples with α = 0.13 and α = 1.65 were not periodic). The SAXS profiles of all of the mesoporous samples with α values in the range 0.22 < α < 0.90, exhibit shoulders in the vicinity of q = 0.1 nm^{-1}. It is reasonable to assume that the SAXS profiles of mesoporous membranes are related primarily to the center-to-center distance of adjacent pores. This is analogous to SAXS profile of the pure block copolymer wherein the primary scattering maximum at q = 0.152 nm^{-1} gives the distance between adjacent 100 planes of PS cylinders. The lack of a well-defined scattering peak indicates the absence of a well-defined periodic structure, suggesting that the internal pore structure is significantly more complex than the surface SEMs suggest. We fit power laws through the data in q < 0.1 nm^{-1} regime and the q > 0.1 nm^{-1} regime. We propose that the intersection of these power law fits is indicative of the characteristic distance between adjacent pores in our mesoporous membranes. The resulting fits for the α = 0.22 sample are shown in Figure 14b, and the intersection is located at $q = q_{SAXS}$ = 0.117 nm^{-1}. We define $d_{SAXS} = 2\pi / q_{SAXS}$, which for the α = 0.22 sample is 53.7 nm. This procedure was repeated for all of the membranes. Table 2 contains a comparison d_{SEM} and d_{SAXS} values of our membranes (d_{280eV} and $d_{284.2eV}$ will be discussed later). It is clear there is a reasonable correspondence between surface morphology (d_{SEM}) seen in Figure 12 and the SAXS profiles seen in Figure 14 (d_{SAXS}). In Figure 14c, we show the SAXS profiles for the SES membranes prior to homopolymer dissolution. These curves were also fit to power laws and $d_{SAXS,UW}$ values are included in Table 2. In the α = 0.22 to 0.44 range, the unwashed and washed d-spacings are similar. There is a shoulder in the q-range from 0.25 to 0.70 nm^{-1}. Pure semicrystalline PE samples exhibit a primary SAXS peak centered around q = 0.18 nm^{-1} and secondary shoulders around 0.36 nm^{-1}.[82] We attribute the scattering shoulder in Figure 14c to scattering from PE crystallites. The shoulders disappear when the SES sample is heated above the melting temperature (data not shown for brevity). The crystalline shoulders are not seen in the mesoporous samples (Figure 14a). We attribute this to the large scattering contrast between voids and PE relative to that between crystalline and amorphous PE. Both the SEM and SAXS data shown thus far for the porous films distinguish only between polymer and voids. We have

not yet addressed microphase separation between the PS and PE blocks in the mesoporous SES copolymer films.

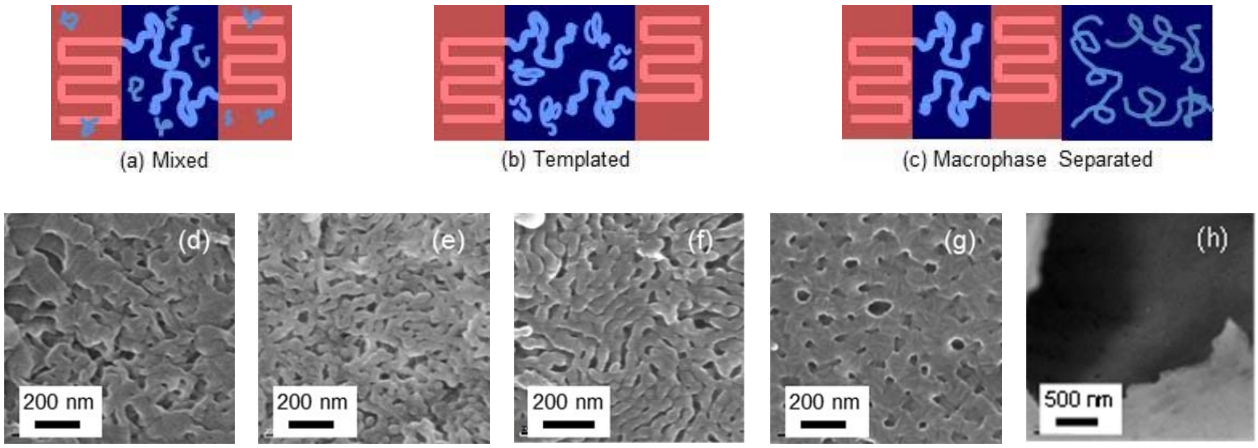

Figure 13. Schematic representations and SEM images of SES membranes.
Schematic representation of homopolymer distribution in SES membrane before washing for a) mixed, b) templated, and c) macrophase separated cases. Scanning electron micrographs of the surfaces of porous SES membranes at normalized chain length of the sacrificial homopolymer d) α = 0.13, e) α = 0.22, f) α = 0.36, g) α = 0.90, h) α = 1.65.

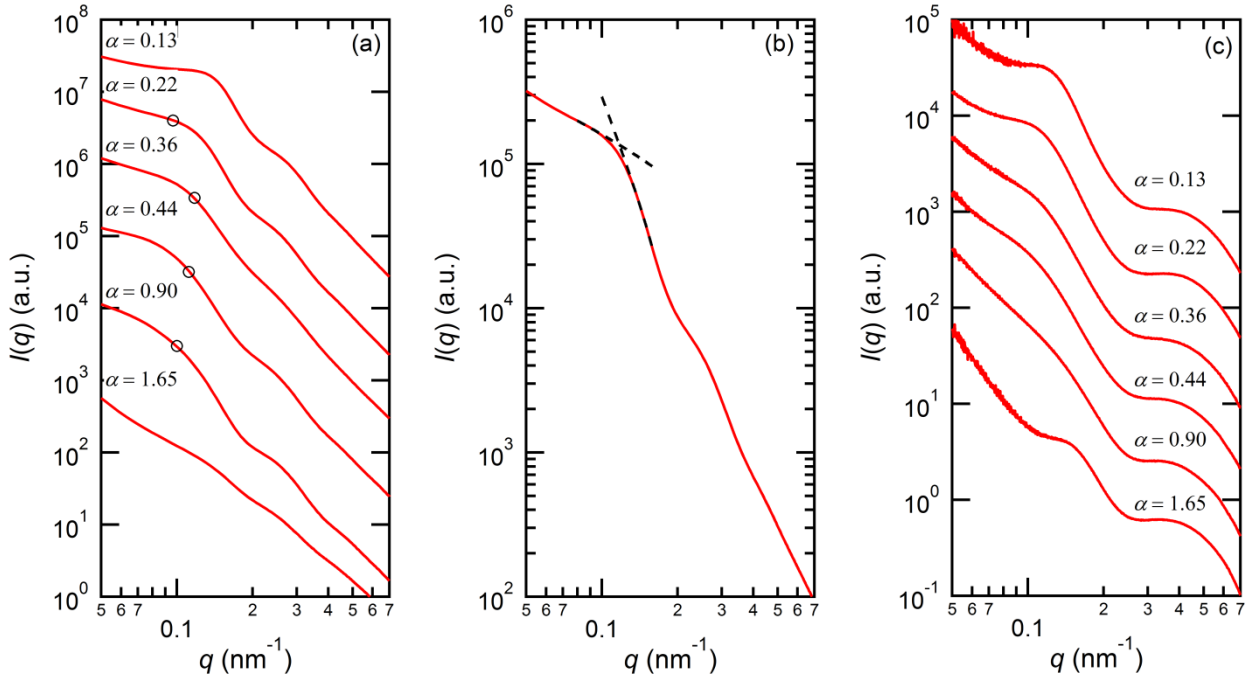

Figure 14. SAXS profiles of SES films before and after washing.
a) SAXS profile of SES films after homopolymer extraction with intensity, $I(q)$ (a.u.), as a function of scattering vector, q (nm^{-1}), at all normalized chain length of the sacrificial homopolymer values, α, studied. The open circles on the profiles with α from 0.22 to 0.90 represents SEM data, $q = 2\pi / d_{\mathrm{SEM}}$.

In b), we show the α = 0.22 profile where the dashed lines represent power law fits below and above q = 0.1 nm^{-1}. c) SAXS profile of SES films before homopolymer extraction with intensity, $I(q)$ (a.u.), as a function of scattering vector, q (nm^{-1}), at all normalized chain length of the sacrificial homopolymer values, α, studied.

RSoXS contrast matching

The complex index of refraction for x-rays, $n(\lambda)$, is given by $n(\lambda) = 1 - \delta(\lambda) + i\beta(\lambda)$, where δ and β are the real and imaginary indices of refraction, respectively. β was determined for PE and PS from existing NEXAFS data.[83] δ was then determined using the Kramer-Kronigs equation. In the hard x-ray regime, which correspond to x-ray energies far away from the absorption edge, δ dominates. δ and β for PS and PE are a strong function of x-ray energy near the carbon K-edge (285 eV). The scattering contrast between two phases, labeled 1 and 2 with refractive indices n_1 and n_2, is given by $C_{1,2} = (n_1 - n_2)^2$. $C_{\mathrm{PS,PE}}$ is thus given by $(\delta_{PS} - \delta_{PE})^2 + (\beta_{PS} - \beta_{PE})^2$, while $C_{\mathrm{PS,Void}}$ and $C_{\mathrm{PE,Void}}$ are given by $(\delta_{\mathrm{PS}})^2 + (\beta_{\mathrm{PS}})^2$ and $(\delta_{\mathrm{PE}})^2 + (\beta_{\mathrm{PE}})^2$, respectively. In Figure 15a, we plot $C_{i,j}$ versus λ, wavelength (nm) or equivalently E, the energy of the incident soft x-rays (eV) ($E = hc/\lambda$, where h is Planck's constant, 4.136 x 10^{-15} eV s, and c is the speed of light, 2.998 x 10^{17} nm s^{-1}). In Figure 15b-d, we show the templated pore geometry with the contrast-matched phases colored in white. As was the case with SAXS, we assume that the RSoXS data indicate the distance between adjacent microphases. At E = 280 eV, $C_{\mathrm{PS,Void}} << C_{\mathrm{PE,Void}}$ and $C_{\mathrm{PS,Void}} << C_{\mathrm{PS,PE}}$, i.e. the PS microphase and void phase are contrast matched as illustrated in Figure 14b. Under these conditions, the primary periodic structure observed is that between adjacent voids, as shown by the bracket in Figure 15b. Similarly, at E = 284.2 eV, $C_{\mathrm{PE,Void}} << C_{\mathrm{PS,Void}}$ and $C_{\mathrm{PE,Void}} << C_{\mathrm{PS,PE}}$, i.e. the PE microphase and void phase are contrast matched as illustrated in Figure 15c. Under these conditions, two periodic structures are evident as indicated by the two brackets in Figure 15c. Both the distance between adjacent voids (left bracket in Figure 15c) and the average distance between adjacent PS domains (right bracket in Figure 15c) are evident under these conditions. At E = 300 eV, well-removed from the carbon K-edge, we have the typical contrast obtained in hard x-ray scattering, $C_{\mathrm{PS,PE}} << C_{\mathrm{PS,Void}}$ and $C_{\mathrm{PS,PE}} << C_{\mathrm{PE,Void}}$, i.e. neither PS nor PE are contrast matched to the voids and scattering is dominated by the distance between adjacent voids.

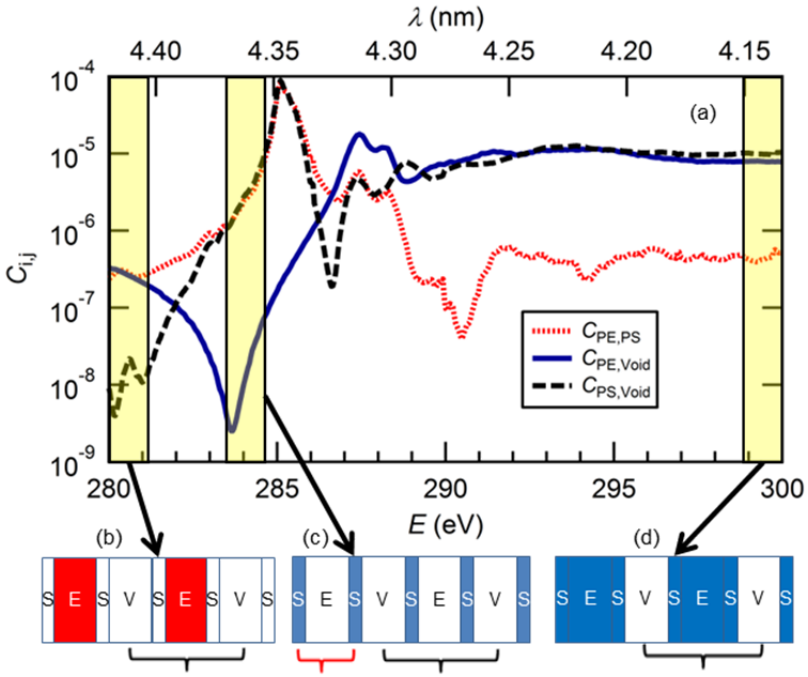

Figure 15. Contrast matching diagrams for RSoXS.
Contrast, $C_{i,j}$, as a function of energy, E and equivalently, wavelength, λ. Three regions are highlighted and graphical representations of the contrast matching are shown for the templated membranes at: b) E = 280 eV ($C_{PS,Void}$ is << $C_{PE,Void}$ and $C_{PS,PE}$), c) E = 284.2 eV ($C_{PE,Void}$ is << $C_{PS,Void}$ and $C_{PS,PE}$), and d) E >300 eV ($C_{PS,PE}$ is << $C_{PS,Void}$ and $C_{PE,Void}$). The letters 'S', 'E', and 'V' stand for PS, PE, and voids, respectively. Brackets represent the periodic structures that are expected to scatter.

In Figure 16a, we present RSoXS and SAXS data for the templated membrane with α = 0.36. The RSoXS data at E = 280 eV contain a shoulder that is similar to the SAXS profile. At this energy, $C_{PE,Void}$ dominates (Figure 15b). We use the two power law fit approach described above to analyze the RSoXS data at E = 280 eV. The value of the characteristic distance between adjacent voids measured by RSoXS at E = 280 eV, d_{280eV} (α = 0.36) is 51.2 nm. This is similar to the d_{SAXS} (α = 0.36) value of 57.9 nm. We see a qualitative change in the RSoXS profile as E is increased towards E = 284.2 eV. At energies above E = 283.4 eV, the shoulder gives way to a well-defined scattering peak. A Gaussian function was used to fit the data in the vicinity of the peak at E = 284.2 eV to give the peak position, q*. The RSoXS-derived characteristic length at E = 284.2 eV, $d_{284.2eV}$ (α = 0.36) is 2π/q* = 38.8 nm.

In order to explain the trends seen in the RSoXS data from the α = 0.36 sample shown in Figure 16a, we refer back to the contrast matching schemes described in Figure 15. We assume that we have voids lined with PS chains as shown schematically as shown in Figure 15b-d. At E = 280 eV, scattering is dominated by the distance between adjacent voids. Eliminating the scattering contribution from the relatively thin pore lining has little effect on scattering. Thus the profiles at E = 280 eV and SAXS (based on hard X-rays) are very similar. On the other hand, at

E = 284.2 eV, both $C_{PS,PE}$ and $C_{PS,Void}$ are significant. Unlike the pore structure that is polydisperse and complex, the block copolymer microphases have a well-defined length scale. We thus see a scattering peak in the E = 284.2 eV scan with $d_{284.2eV}$ = 38.8 nm, similar to d_{BC} = 41.3 nm. This peak is superposed on the void-dominated scattering profile due to the relatively large value of $C_{PS,Void}$. The net result is a non-monotonic scattering profile with void scattering dominating data in the low-q regime (q < 0.15 nm^{-1}), and PS/PE microphase separation dominating the high-q regime (q > 0.15 nm^{-1}). The fact that $d_{284.2eV}$ and d_{BC} are similar indicates that in templated mesoporous films, the block copolymer chains are not distorted, relative to the neat nonporous SES copolymer film. *The ability of RSoXS to study both the pore structure and microphase separation of the block copolymer is an important new finding of the present study*.

In Figure 16b, we present RSoXS and SAXS data for the macrophase separated sample with α = 1.65 film. Unlike the α = 0.36 film (Figure 16a), the SAXS data and the E = 280 eV RSoXS are very different. The absence of a shoulder in the SAXS data suggests the presence of pores with no characteristic length scale. In contrast, the E = 280 eV RSoXS data contain a well-defined shoulder. This indicates that the schematic diagrams in Figure 15 b-d do not apply to this sample. Macrophase separation results in a separate periodic phase comprised of the pure block copolymer which can be observed due to the relatively large value of $C_{PS,PE}$. This is confirmed by the RSoXS patterns obtained as a function of increasing energy. Most of the RSoXS scattering profiles contain a well-defined peak. In this case, we find d_{280eV} (α = 1.65) = 39.3 nm and $d_{284.2eV}$ (α = 1.65) = 39.2 nm, which are similar to d_{BC}. We conclude that in porous films made from macrophase separated systems, the block copolymer chains are not distorted, relative to the neat nonporous SES copolymer film.

A comparison of Figure 16a and b suggests the non-intuitive result that the presence of well-defined scattering features in RSoXS at energies between E = 283.4 and 284.2 eV, with characteristic length scales similar to that of the pure block copolymer, is not indicative of a templated mesoporous membrane. Instead, the presence of a shoulder at E = 280 eV that gradually gives way to a peak at E = 284.2 eV, where $d_{284.2eV} = d_{BC}$ is a signature of a templated mesoporous membrane.

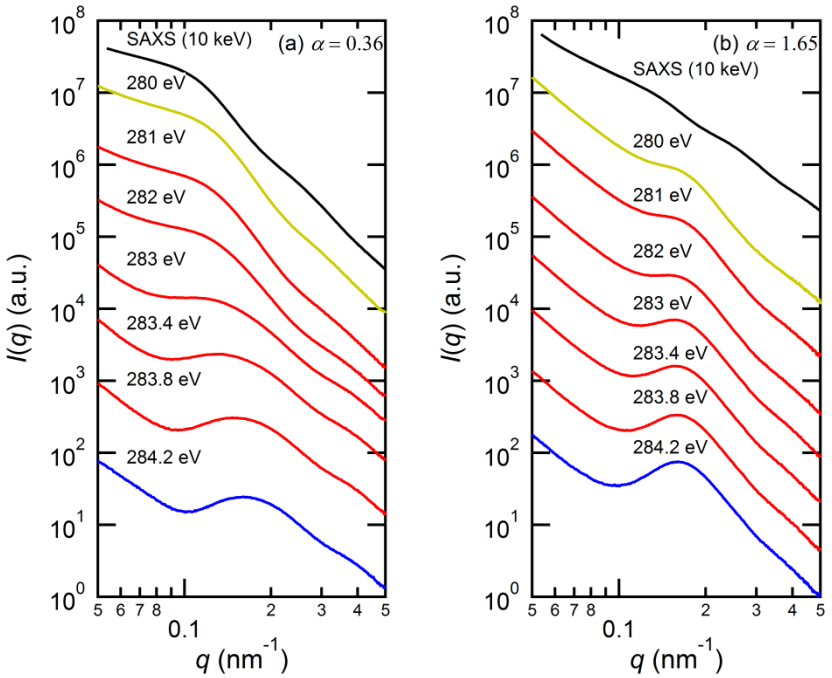

Figure 16. Scattering profiles of porous SES films at different energies.
X-ray scattering profiles of porous SES films with intensity, $I(q)$, as a function of scattering vector, q at normalized chain length of the sacrificial homopolymer values, a) $\alpha = 0.36$ and b) $\alpha = 1.65$. In both figures, from top to bottom, the first curve represents the SAXS profile, followed by RSoXS profiles with energy increasing from $E = 280$ eV to $E = 284.2$ eV. The profiles at $E = 280$ eV and $E = 284.2$ eV are plotted in different colors.

The analysis of the SAXS and RSoXS data described above was repeated for all of the samples listed in Table 1, and the results of this exercise are shown in Table 2 where d_{SEM}, d_{SAXS}, d_{280eV}, and $d_{284.2eV}$ are given. In all cases, d_{SAXS} is slightly larger than d_{280eV}. The finite value of $C_{PS,PE}$ at $E = 280$ eV results in non-negligible contributions in RSoXS due to microphase separation. It is because of this that the scattering features shift to slightly higher q. In all cases except $\alpha = 1.65$, $d_{284.2eV}$ is significantly smaller than d_{280eV}.

In Figure 17a, we plot RSoXS data at $E = 280$ eV for all films studied. The curves in Figure 17a have similar shape to the SAXS profiles in Figure 14, with the exception of the $\alpha = 1.65$ film that we have already discussed. Quite surprisingly, there is no qualitative difference in the RSoXS data at $E = 280$ eV obtained from the mixed case ($\alpha = 0.13$) and the templated cases ($\alpha = 0.22$ - 0.44) in Figure 17a. It is evident that the $E = 280$ eV RSoXS data are not affected by the large effect of pore-connectivity seen in the conductivity data in Figure 12.

In Figure 17b, we plot RSoXS data at $E = 284.2$ eV for all films studied. We see that all of the profiles are dominated by a peak corresponding to microphase separation between PS and PE. At α values between 0.22 and 1.65, $d_{284.2eV}$ is approximately 39.0 nm, which is similar to the d_{BC} of 41.3 nm. In the $\alpha = 0.13$ case, however, $d_{284.2eV} = 33.5$ nm, which is significantly smaller than d_{BC}. This corresponds to the mixed case wherein the PS homopolymer is uniformly

distributed in both PS-rich and PE-rich microphases. We propose that in the α = 0.13 PS/SES film prior to dissolution, the PS homopolymer chains are able to penetrate the PE-rich microphase d_{SAXS} (α = 0.13) = 44.9 nm. Subsequent dissolution of these PS chains reduces the size of the PE domains. The clearest signature of the mixed case is thus contained in the RSoXS data at E = 284.2 eV.

Table 2. Domain spacings determined by SAXS, SEM, and RSoXS.*

α	d_{SAXSUW} (nm)	d_{SEM} (nm)	d_{SAXS} (nm)	d_{280eV} (nm)	$d_{284.2eV}$ (nm)
0.13	51.1	-	44.9	44.1	33.5
0.22	56.6	65.1	53.5	51.5	38.5
0.36	55.4	53.4	57.9	51.2	38.8
0.44	57.7	56.3	64.1	53.6	38.8
0.90	-	62.9	69.4	61.4	39.1
1.65	41.3	-	-	39.3	39.2

* d_{SEM} were calculated using line profiles, d_{SAXSUW}, d_{SAXS}, and d_{280eV} were calculated from power law fits, and $d_{284.2eV}$ was calculated by fitting a Gaussian to the data. Typical uncertainty in the tabulated length scales is 2 nm. The proposed approach failed to give robust domain spacings in samples with extremely weak shoulders (-).

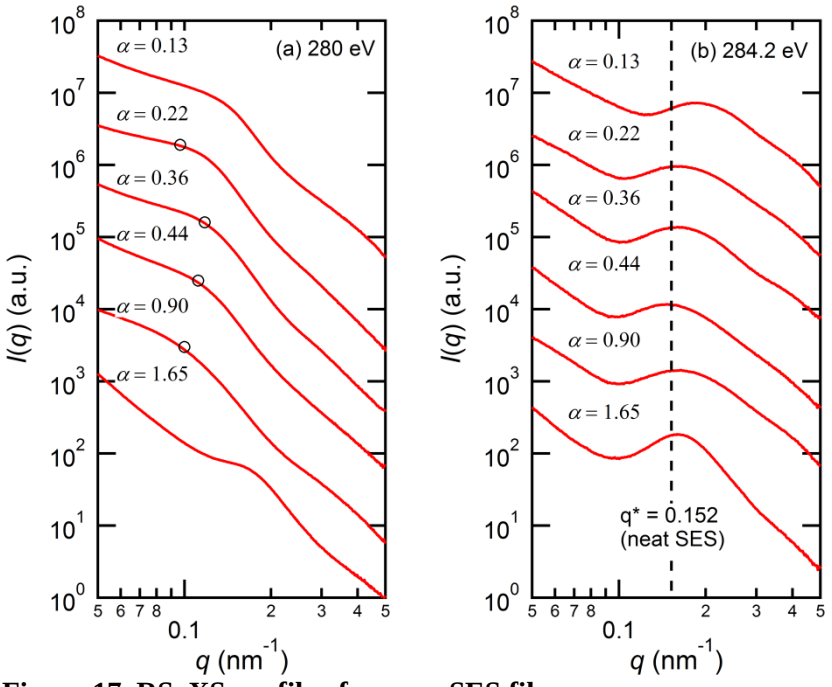

Figure 17. RSoXS profile of porous SES films.
The intensity, $I(q)$, is plotted as a function of scattering vector, q at all values of the normalized chain length of the sacrificial homopolymer, α, studied at a) E = 280 eV and b) E = 284.2 eV. In a), the open

circles on the profiles with α from 0.22 to 0.90 represents the primary peak, q^*, determined from the line profiles of SEM images. In b), the vertical dashed line at q = 0.152 nm^{-1} represents the primary scattering peak of the neat SES copolymer.

3.4 Conclusions

Contrast-matched RSoXS experiments were performed on mesoporous polystyrene-*block*-polyethylene-*block*-polystyrene (SES) copolymer membranes to independently study block copolymer microphase separation and polymer-void structure. Mesoporous SES membranes were generated by blending an SES copolymer with polystyrene (PS) homopolymer and then using a selective solvent to remove the PS homopolymer. This resulted in a membrane with three distinct phases: PS, PE, and voids. In the ideal scenario, the PS homopolymer chains are contained within the polystyrene-rich microphase, and the removal of these chains results in pores lined with the PS block of the SES copolymer. We refer to this as the templated morphology. Ionic conductivity measurements on mesoporous membranes soaked in a conventional electrolyte confirm that the pores are well-connected when the pores are templated. The morphology of these membranes was studied using SAXS and SEM, but these techniques are sensitive only to the contrast between polymer and voids. The main purpose of this chapter is to demonstrate that block copolymer microphase separation can be studied using RSoXS in spite of the fact 43% of the sample is occupied by mesoscale voids. RSoXS thus enables complete characterization of the morphology of mesoporous films when our strategy for templating succeeds and when it fails.

Chapter 4 – Effect of Non-Solvent Exposure on Morphology of Mesoporous Semi-crystalline Block-Copolymer Films

Abstract

Polystyrene-*block*-polyethylene-*block*-polystyrene (SES) copolymers were blended and homopolymer polystyrene (PS), and films of the blend were cast using a doctor blade. The non-porous SES and PS films were exposed to both tetrahydrofuran (THF) and methanol (MeOH) in an alternating fashion for one-minute intervals three times, without letting the films dry between solvents. At this point, films were either removed from the MeOH and dried, or the films were immersed in THF and then dried. THF is a non-solvent for crystalline polyethylene (PE), but a good solvent for both amorphous PE and PS. Methanol is a non-solvent for semi-crystalline PE, amorphous PE, and PS. Films that were dried with MeOH as the final non-solvent were highly porous and exhibited high conductivity when swollen in a liquid electrolyte. In contrast, films that were dried with THF as the final non-solvent were non-porous and exhibited poor conductivity when swollen in a liquid electrolyte. We study the underpinnings of the non-solvent treatment effects using electron microscopy, nitrogen physisorption, and x-ray scattering techniques.

4.1 Introduction

Mesoporous polymer membranes are often composed of semi-crystalline polymers. These membranes are often made by first creating a heterogeneous nonporous film containing soluble oligomers or polymers. The mesoporous void structure is created in a second washing step by dissolving away the soluble components. An example of such a process is that polyethylene and polypropylene battery separators are made by first making films containing waxy hydrocarbons and high molecular weight polymers and then dissolving away the waxy component.[1-3] The separator is the most expensive component of a lithium-ion battery per unit mass,[4] and virtually the entire cost of this component is due to processing (raw material costs are negligible). Semi-crystalline polymers such as polyethylene and polypropylene are generally insoluble at temperatures well-below the crystalline melting temperature. Thus, in principle, virtually any solvent can be used to dissolve out the soluble species. However, all solvents are effectively non-solvents for the semi-crystalline polymer. The problem arises because all semi-crystalline polymers contain significant volume fractions of non-crystalline regions.[84, 85] These regions can be attacked by solvents, and subtle rearrangements from such attacks might significantly affect the geometry of the pores that are left behind. This can have a significant impact on the performance of mesoporous films. The purpose of this chapter is to explore the relationship between non-solvent exposure and morphology of model mesoporous films that are primarily made up of polyethylene.

This chapter is part of a series on the synthesis and characterization of mesoporous block copolymer films. The procedure used to make the films was described in Chapters 1 and 2.[69] In Chapter 3, we used resonant soft x-ray scattering to characterize both the void structure and microphase separation.[86] The membranes are synthesized by first blending a symmetric polystyrene-*block*-polyethylene-*block*-polystyrene (SES) copolymer with homopolymer polystyrene (PS). Films of the blend are then cast using a doctor blade. Tetrahydrofuran (THF) is a solvent for PS, but is a non-solvent for crystalline polyethylene (PE). We create mesoporous films by first exposing the SES/PS blend to THF and then to methanol (MeOH), a non-solvent for PS, amorphous PE, and crystalline PE. We use a variety of techniques to characterize microphase separation and the void structure in films exposed to THF and MeOH: AC impedance spectroscopy on membranes soaked with an electrolyte, scanning electron microscopy, nitrogen physisorption, small angle x-ray scattering, and resonant soft x-ray scattering. These characterization experiments provide an understanding of the microscopic processes that occur when the films are exposed to the non-solvents of interest and how these processes affect macroscopic transport through the films.

4.2 Experimental

Most of the characterization techniques used in this chapter are described in Chapter 1. Small angle x-ray scattering (SAXS) data were normalized using an absolute intensity calibrant and these methods are described below.

Polymers used

The molecular weights of the PS and PE blocks for the SES copolymer were 13.5 and 67 kg mol^{-1}, respectively, and the PE volume fraction, $\phi_{PE,BCP}$, was 0.75 (in the melt state at 140 ^{o}C). The melt density of the SES is 0.83 g cm^{-3} at 140 ^{o}C.[11]

Small Angle X-ray Scattering

Absolute intensity SAXS experiments were used to characterize the morphology of the SES membranes. Measurements were performed on beam line 7.3.3 at the Advanced Light Source at Lawrence Berkeley National Laboratory and beam line 1-4 of the Stanford Synchrotron Radiation Laboratory. Samples were stacked to a thickness of between 100 and 300 μm to increase the scattering volume. The thickness of individual films was measured using a micrometer. No windows were needed to contain the samples. A silver behenate sample was used as a standard, and data were reduced using the Nika program for Igor Pro available from Jan Ilavsky at the Advanced Photon Source (APS).[15] The azimuthally averaged scattering intensity, I, was recorded as a function of the scattering vector q ($q = 4\pi \sin(\theta/2)/\lambda$), where θ is the scattering angle and λ is the wavelength of the incident beam.

The intensities of the scattered X-rays were normalized using a 1.0 mm thick glassy carbon sample (sample M30) provided by Jan Ilavsky at the APS.[87] Sample exposure times varied from 1 to 60 seconds. Glassy carbon and empty cell data were collected at each exposure time used. The corrected intensity, $I_{cor}(q)$, was calculated by

$$I_{cor}(q) = \frac{I_{raw}(q)/T - I_{MT}(q)}{(t)(\tau)} \quad (4)$$

where $I_{raw}(q)$ is the raw measured intensity, $I_{MT}(q)$ is the measured empty cell intensity, t is the thickness of the sample in mm, τ is the sample exposure time, and T is the sample transmission normalized by the empty cell.

The absolute SAXS intensity, $I_{SAXS}(q)$, was calculated by

$$I_{SAXS}(q) = I_{cor}(q)\eta \quad (5)$$

where η is the scaling factor for the glassy carbon at a given exposure time and was calculated by

$$\eta = \frac{I_{abs,cal,GC}(q)}{I_{cor,GC}(q)} \quad (6)$$

where $I_{abs,cal,GC}(q)$ is the calibrated glassy carbon intensity provided with the standard and $I_{cor,GC}(q)$ is the scattering profile measured in our instrument and corrected using Equation 1. As expected, η was independent of q. More detailed discussions of absolute intensity calibrations can be found elsewhere.[88, 89]

Error analysis

The conductivity data reported are the average of at least 4-5 measurements. In the case of the x-ray scattering and SEM studies, experiments were repeated to verify results; we present only one set of data. Data from both techniques were used to determine characteristic length scales of the morphology of our system. The observed variance in the length scales determined was 2 nm.

4.3 Results and discussion

Dried, nonporous SES/PS films with PS occupying 43% of the film by volume were first immersed in THF to dissolve out PS homopolymer chains. This was followed by immersing the film in MeOH. Our standard protocol was to repeat the THF and MeOH immersions three times. Each immersion step lasted for 1-2 min and the films were wet when they were transferred from one solvent to the other. We refer to these films as the methanol-washed films (SES-M), referring to the fact that the last washing step involved the non-solvent methanol. A second set of films were created by using an additional THF-immersion step immediately following the three THF and MeOH immersions described above. We refer to these films as the THF-washed films

(SES-T), referring to the fact that the last washing step involved the non-solvent THF. Note that SES-M films have been exposed to THF, and SES-T films have been exposed to MeOH; the only difference is the final washing step. All films were dried at 25 ^{o}C in a vacuum oven for 4 hours.

The samples discussed in this study are summarized in Table 1. In all of the films, the void fraction, ϕ_V is fixed at 0.43, the volume fraction of PE in the mesoporous films is also 0.43, and the volume fraction of PS in the mesoporous films is 0.14. The mesoporous films are distinguished by the molecular weight of the sacrificial PS homopolymer, α, and the final non-solvent treatment. The only distinction between the films thus related to components that were completely removed in the processing steps. In our previous study, we demonstrated the importance of α. Highly connected mesoporous films that are templated by block copolymer self-assembly are obtained only at intermediate values of α between 0.2 and 0.5. When α is below this range, the PS homopolymer is soluble in both PS and PE microphases of the block copolymer, and when it is above this range, we obtain macrophase separation between the block copolymer and the homopolymer.

Table 3 shows the results of electrolyte uptake in our mesoporous films. ϕ_{elec} is the volume fraction of electrolyte taken up by the swollen film, and is given by $(m_{swollen} - m_{dry})(1-\phi_V)/[\rho_{elec}(m_{dry}/\rho_{poly})]$, where m_{dry} and $m_{swollen}$ are the dry and swollen weights of the film, ρ_{elec} = 1.26 g cm^{-3}, is the density of the liquid electrolyte (1.0 M $LiPF_6$ in EC/DEC, 1:1 v/v), and ρ_{poly} = 0.83 g cm^{-3} is the density of the SES copolymer in the melt state. For the case of the SES-M films, ϕ_{elec} is similar to ϕ_V over a wide range of α values. At α between 0.22 and 0.44, ϕ_{elec} values of the SES-M samples range from 0.47 to 0.51. Values of ϕ_{elec} obtained from the SES-T samples are significantly lower than those obtained from the SES-M samples, with the exception of the macrophase separated sample obtain at α = 1.65. At α between 0.22 and 0.44, ϕ_{elec} values of the SES-T samples range from 0.15 to 0.29. This means that the void volume accessible to the electrolyte in SES-T films is significantly less than in SES-M films. In the SES-M samples, ϕ_{elec} is a maximum at an intermediate α value of 0.44. In contrast, in the SES-T samples, ϕ_{elec} increases monotonically with α.

Table 3. All samples studied in this chapter.*

Sample	α	$M_{n,sacrificial,PS}$ (kg mol^{-1})	ϕ_{Elec}
SES-M	0.13	1.7	0.30 ± 0.07
SES-M	0.22	3.0	0.48 ± 0.05
SES-M	0.37	4.8	0.47 ± 0.05
SES-M	0.44	5.9	0.51 ± 0.05
SES-M	0.90	12.2	0.40 ± 0.07
SES-M	1.65	22.3	0.35 ± 0.02

SES-T	0.13	1.7	0.10 ± 0.04
SES-T	0.22	3.0	0.15 ± 0.04
SES-T	0.37	4.8	0.16 ± 0.03
SES-T	0.44	5.9	0.29 ± 0.06
SES-T	0.90	12.2	0.32 ± 0.04
SES-T	1.65	22.3	0.34 ± 0.08

* The normalized chain length of the sacrificial homopolymer, α, is calculated relative to the PS block of the SES copolymer, which is 13.5 kg mol^{-1}. Other variables listed in the table are: molecular weight of the sacrificial homopolymer PS, $M_{n,sacrificial,PS}$ and volume fraction of electrolyte uptaken, ϕ_{Elec}.

The importance of the washing step is also clear in Figure 18, where we plot ionic conductivity, σ, versus α for the washed films listed in Table 3 after they were soaked in electrolyte. The open squares in Figure 18 show data obtained from SES-M samples. Conductivity exhibits a sharp maximum in the vicinity of α = 0.3. The filled circles in Figure 18 show conductivity data obtained from SES-T samples. Regardless of the value of α, conductivity in SES-T films is significantly less than that of SES-M films. This is consistent with the electrolyte uptake data given in Table 3.

It is clear from the data in Table 3 and Figure 18 that the mesoporous morphology obtained in the SES films after the MeOH wash is destroyed by a subsequent THF wash. This is somewhat surprising as these films have been exposed to THF several times in both processing protocols. It also suggests that the destruction and recreation of the porous structure in the presence of THF and MeOH is reversible. In order to confirm this, we took the SES-T films, rinsed out the electrolyte using THF, and immersed these films in MeOH. We refer to these films as SES-M', and conductivity data obtained from these films after drying and reswelling with electrolyte are shown by filled triangles in Figure 18. The conductivities of the SES-M' films are very similar to those obtained from SES-M films, confirming the reversibility of pore creation and destruction induced by non-solvent treatment steps.

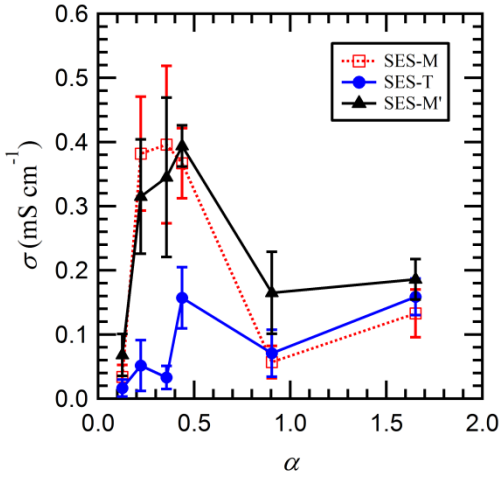

Figure 18. Ionic conductivity of SES-T and SES-M films.

Ionic conductivity, σ, of mesoporous SES films soaked in 1.0 M $LiPF_6$ in EC/DEC 1:1 v/v as a function of the normalized chain length of the sacrificial homopolymer, α.

In Figure 19a and b, we show the cross sectional SEM images of the SES-M and SES-T films for the α = 0.36 film. The SES-M film exhibits a highly connected porous structure throughout the entire film. The highly porous nature of the film allows significant electrolyte uptake and leads to high conductivity. In the SES-T film we see only a few isolated and unconnected pores. This void structure is incapable of significant electrolyte uptake and leads to low conductivity.

Our hypotheses for the morphologies of the SES-M and SES-T films are shown in Figure 19c and d. The SES-M film (Figure 19c) contains three phases: a semi-crystalline phase composed of amorphous and crystalline PE regions, an amorphous PS phase that lines the void, and a central void. We propose that exposing this film to THF, a good solvent for both PS and amorphous PE, results mainly in the rearrangement of the amorphous PE segments as shown in Figure 19d. These amorphous segments fill out the void space that was present in the SES-M films. It is important to note that the illustrations in Figure 19c and d are simplified one-dimensional representations of the complex porous structures in our system. The main points that Figure 19d illustrates are that exposure to THF results in a reduction of pore volume and destruction of the templated pore structure obtained after exposure to MeOH. The remainder of the paper is devoted to morphological characterization that supports the hypotheses presented in Figure 19c and d.

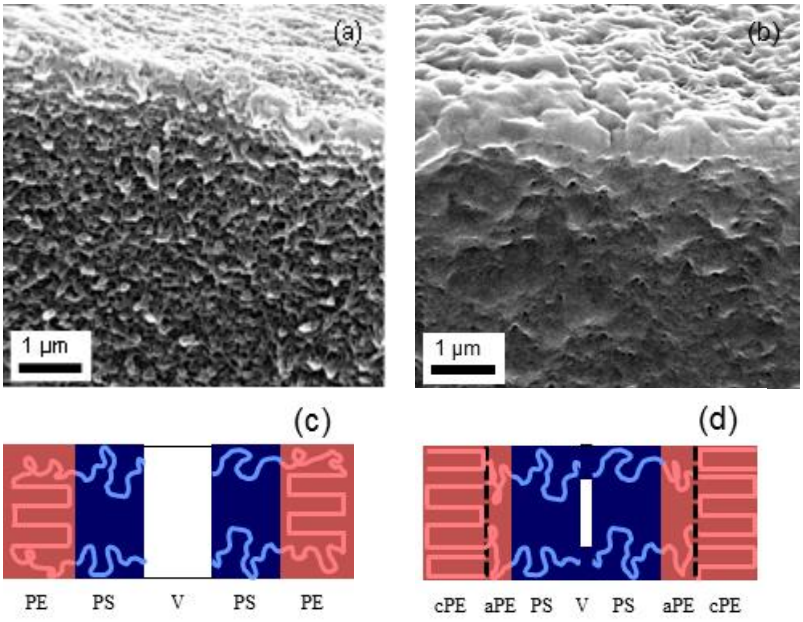

Figure 19. SEM images and schematics of SES-M and SES-T films.
Scanning electron micrographs of the surfaces of porous SES membranes at α = 0.36 for the a) SES-M and b) SES-T films. Schematic representation of the c) SES-M and d) SES-T films. Phases are labeled below the schematic representations: polyethylene (PE), polystyrene (PS), void (V), crystalline PE (cPE), and amorphous PE (aPE).

In Figure 20, we plot absolute SAXS intensity, I_{SAXS}, as a function of q for the $\alpha = 0.36$ samples. In addition to the SES-M and SES-T films, we show data obtained from the SES/PS mixture prior to extraction of the PS chains. The profiles are presented with no vertical shift. It is evident that exposing the SES/PS films to the standard PS protocol of three alternating rinses in THF and MeOH results in a dramatic increase of I_{SAXS} (compare SES/PS and SES-M data in Figure 20). Exposing the SES-M film to THF results in a SAXS profile that is similar to the SES/PS film that contains no voids. It is thus reasonable to conclude that the SES-T films contain much fewer voids than the SES-M as Figure 19c and d suggest.

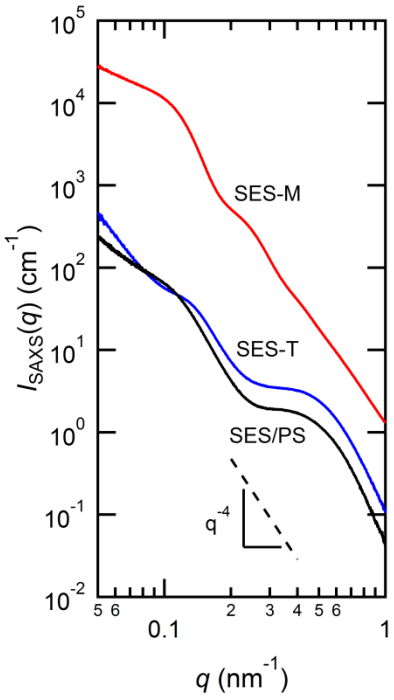

Figure 20. SAXS profile of SES films before and after homopolymer extraction.
The intensity, I, is plotted as a function of scattering vector, q at $\alpha = 0.36$. The dotted line represents a q^{-4} slope.

In samples with sharp interfaces, I_{SAXS}, in the limit of high q, is given by Porod's law,

$$I_{SAXS}(q) = \frac{2\pi(\Delta b)^2 a_{s,P}}{q^4} \text{ as } q \to \infty \qquad (7)$$

where Δb is the scattering length density difference between the polymer and void and $a_{s,P}$ is the area of the polymer/void interface per unit volume determined from Porod's law.[81] We have assumed in this analysis that the main scattering contrast is between the void and the polymer and not between the PS and PE. We approximate the scattering length density difference

between polymer and void, Δb = 9.2x10^{-4} nm^{-2} by taking the volume averaged scattering length density of PS and PE, 9.0x10^{-4} and 9.7x10^{-4} nm^{-2}, respectively.[90] The scattering length density of voids is 0 nm^{-2}. The I_{SAXS} vs q data in Figure 20 from all three samples exhibit Porod scattering in the high q limit. We fit the SES-T and SES-M data in this limit to Porod's law, which gives $a_{s,P}$ for these two samples. We do not fit the SES/PS data as these films are not porous and Δb is thus not appropriate. The values of $a_{s,P}$ for SES-M and SES-T are 1.99x10^{7} and 3.42x10^{6} m^{-1}, respectively. $a_{s,P}$ data were converted to a specific surface area, a_s, using the porous SES membrane density, ρ_{mem} = 0.47 g cm^{-3} (calculated from the melt densities specified in the Experimental Section, with ϕ_V = 0.43). The value of a_s was determined for all of the samples listed in Table 3 using this approach. Another estimate of the a_s for the SES-M films was determined using the BET equation and nitrogen physisorption experiments as described in our previous publication.[13, 69] Nitrogen physisorption experiments on SES-T films did not yield appreciable surface absorption, and we therefore do not report BET values for the SES-T films. This implies that the SES-T films are not very porous.

In Figure 21, we plot specific surface area, a_s, as a function of α for the SES-M films obtained from both nitrogen physisorption data and SAXS data. There is reasonable agreement between the two set of data. The highest values of specific surface areas are obtained at α values between 0.2 and 0.5 for the SES-M membranes. The values of a_s determined from the SES-T films are below 10 m^2/g regardless of the value of α. It is perhaps worth noting that these values of a_s represent an upper bound for the true polymer-void surface area in SES-T films. As noted in Figure 20, the SAXS profiles in SES-T and SES/PS films are similar. Since there are no voids in SES/PS films, the interfaces seen at high q in these films must be due to scattering between PS and PE domains or between crystalline and amorphous PE domains. It is thus very likely that a significant fraction of the Porod scattering seen in SES-T films does not arise from polymer-void interfaces.

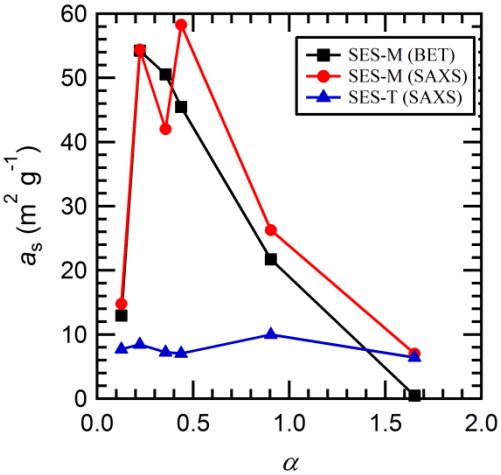

Figure 21. Specific surface areas of SES-M and SES-T films.

Specific surface area, a_s, as a function of the normalized chain length of the sacrificial homopolymer, α for surface areas calculated both from the BET equation and SAXS data in both SES-T and SES-M films.

RSoXS scattering profiles from SES-T and SES-M films with α = 0.36 at E = 280.0 eV and E = 284.2 eV are shown in Figure 22a. In a previous study, we have identified E = 280.0 eV as the energy at which PS is contrast matched to the voids, and E = 284.2 eV as the energy at which PE is contrast matched to the voids. Simplified morphologies of SES-M films under the contrast matching conditions of interest are also shown in Figure 22b and c. The two contrast matched phases are shown in white in these morphologies. The SES-M films show relatively large voids templated by the SES copolymer (Figure 22b and c). At E = 280.0 eV, I_{RSoXS} is dominated by the scattering contrast between PE domains and the other components of the film (PS and void). The characteristic length obtained at this energy, $d_{280.0}$, is the average center-to-center distance between adjacent voids (which is equal to the average center-to-center distance between adjacent PE domains), see Figure 22b. Using the methodology used in Chapter 3,[86] we obtain $d_{280.0eV}$ = 51 nm for the SES-M film. At E = 284.2 eV, I_{RSoXS} is dominated by the scattering contrast between PS domains and the other components of the film (PE and void). The characteristic length, $d_{284.2eV}$, obtained at this energy is the average center-to-center distance between adjacent PS domains, see Figure 22c. Using the methodology used in Chapter 3,[86] we obtain $d_{284.2}$ = 39 nm for the SES-M film. The substantial difference between $d_{280.0}$ and $d_{284.2}$ is noteworthy.

Simplified morphologies of SES-T films under the contrast matching conditions of interest are also shown in Figure 22d and e. The main difference between SES-M and SES-T films are that the SES-T films have a negligibly small void fraction. The voids that were present in the SES-M films are essentially filled by amorphous PE chains in Figure 22d and e. The RSoXS data obtained from SES-T films is qualitatively differently from SES-M films. The characteristic length scales determined from analysis of RSoXS data are $d_{280.0eV}$ = 49 nm and $d_{284.2eV}$ = 54 nm, consistent with the simplified morphologies in Figure 22d and e. In other words, the lack of a substantial difference between $d_{280.0}$ and $d_{284.2}$ is noteworthy.

RSoXS data from all of the samples listed in Table 3 were analyzed using the methodology described above and are summarized in Table 4. In the discussion below we focus on the range of α values where templated mesoporous films are obtained in the SES-M samples ($0.22 \leq \alpha \leq 0.44$). In the case of the templated SES-M films, $d_{280.0eV}$ and $d_{284.2eV}$ values are different; the average difference between $d_{284.2eV}$ and $d_{280.0eV}$ is ~12 nm. The values of $d_{280.0eV}$ represent scattering from adjacent voids, while the values of $d_{284.2eV}$ correspond to the neat block copolymer domain size, d_{BC}, of 41 nm. In the SES-T films, for this same α range described above ($0.22 \leq \alpha \leq 0.44$), the average difference between $d_{284.2eV}$ and $d_{280.0eV}$ is ~4 nm. The values of $d_{280.0eV}$ and $d_{284.2eV}$ are similar to each other and are significantly larger than d_{BC}. Quite surprisingly, $d_{284.2eV}$ and $d_{280.0eV}$ values of the SES-T films are similar to $d_{280.0eV}$ values of the SES-M films. We take this as confirmation of our hypothesis: the overall dimensions and domain sizes of our mesoporous system are constrained by the crystalline part of the PE block,

while the amorphous PE block, which is soluble in THF, fills the pores after the THF wash as shown in Figure 22 b-e.

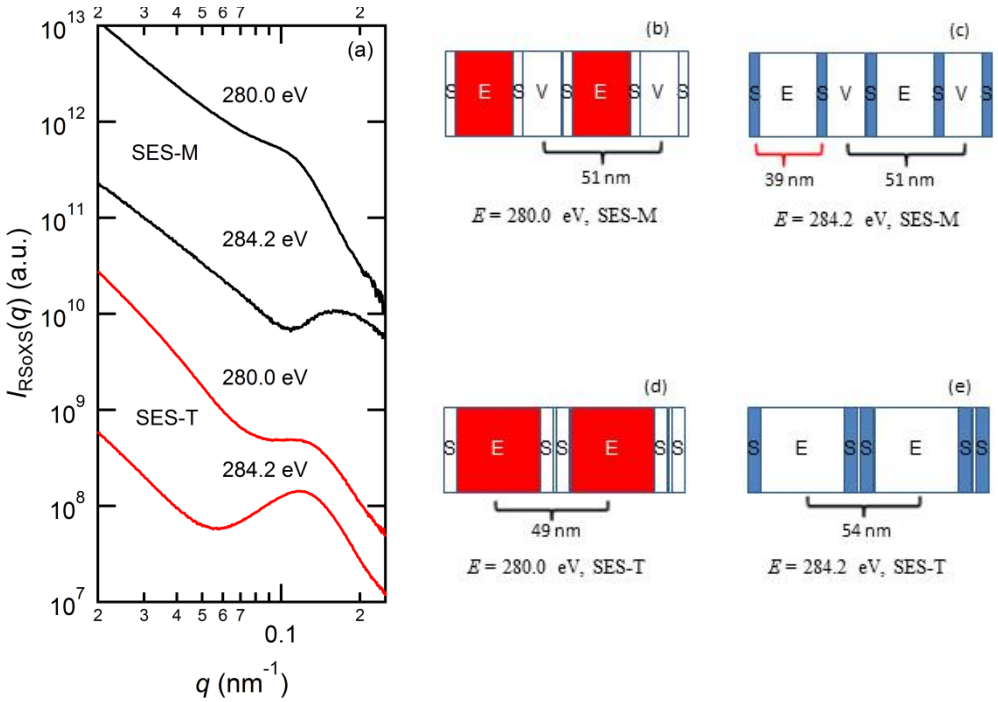

Figure 22. RSoXS profile of SES-T and SES-M (α = 0.36) films.
The intensity, $I(q)$, is plotted as a function of scattering vector, q, at E = 280 eV and E = 284.2 eV.

Table 4. Domain sizes determined by RSoXS for SES-T and SES-M films.*

α	SES-M $d_{280.0eV}$ (nm)	SES-M, $d_{284.2eV}$ (nm)	SES-T, $d_{280.0eV}$ (nm)	SES-T, $d_{284.2eV}$ (nm)
0.13	44.1	33.5	45.9	46.0
0.22	51.5	38.5	46.6	53.5
0.36	51.2	38.8	49.2	53.6
0.44	53.6	38.8	57.6	57.8
0.90	61.4	39.1	52.8	61.0
1.65	39.3	39.2	50.1	47.2

* d_{280eV} was calculated from power law fits, and $d_{284.2eV}$ was calculated by fitting a Gaussian to the data. Typical uncertainty in the tabulated length scales is 2 nm.

4.4 Conclusions

The effect of different non-solvent treatments on the morphology and conductivity of mesoporous semi-crystalline block copolymer films has been studied. A mesoporous polystyrene-block-polyethylene-block-polystyrene copolymer, where the pores are lined with the PS block of the copolymer, was exposed in an alternating fashion to two different non-solvents:

tetrahydrofuran (THF) and methanol (MeOH). If the final solvent treatment used was MeOH, a non-solvent for amorphous PE, crystalline PE, and PS, a porous, highly conductive (in the presence of liquid electrolyte) film was formed. If instead, the final solvent treatment used was THF, a non-solvent for crystalline PE, but a good solvent for amorphous PE and PS, a non-porous film with low conductivity (in the presence of liquid electrolyte) was formed. Interestingly, we have found that the change between non-porous and porous films was reversible. We attribute these changes in the conductivity and morphology to the rearrangement of the amorphous PE into the pores, and use contrast-matched resonant soft x-ray scattering (RSoXS) to prove this. The main purpose of this chapter is to demonstrate the dramatic effect different non-solvents can have on the morphology and subsequent properties of mesoporous semi-crystalline block copolymers.

Chapter 5 – Mesoporous Block Copolymer Battery Separators: Molecular Weight Effects and Benchmarking Experiments

Abstract

Mesoporous block copolymer battery separators were tested and benchmarked against a commercial battery separator. The battery separators were synthesized by blending copolymer polystyrene-*block*-polyethylene-*block*-polystyrene (SES) with a sacrificial homopolymer polystyrene (PS), casting a film of this blend, and then selectively removing the PS homopolymer. Separators were made using three different SES copolymers, which were synthesized with identical PS block length (13.5 kg mol^{-1}), while the PE block length that varied between 47 and 112 kg mol^{-1}. The conductivity (in a liquid electrolyte) of each of the mesoporous copolymers was optimized using different molecular weight sacrificial homopolymers and compared favorably to the commercial battery separator. The optimized SES separators were benchmarked against the commercial separator using both tensile strength experiments and full cell battery cycling experiments.

5.1 Introduction

In two recent publications, we have been studying and characterizing mesoporous block copolymer battery separators.[69, 86] The mesoporous block copolymer battery separators are synthesized by blending polystyrene-*block*-polyethylene-*block*-polystyrene (SES) copolymer with homopolymer polystyrene (PS) and solvent casting a nonporous film. The homopolymer PS segregates preferentially to the styrene phase of the block copolymer. We wash out the homopolymer PS using tetrahydrofuran, which can solvate the PS, but cannot solvate the semi-crystalline polyethylene (PE). This results in a porous SES copolymer, whereby the holes are lined with PS chains. Our process is analogous to the wet process of making battery separators,[3] whereby high-molecular-weight semi-crystalline polyolefins are blended with low-molecular-weight amorphous polyolefins, which can be extracted to make pores. Our process differs from the traditional wet process for making battery separators in two key regards: our pores are lined with PS, which can gel in the presence of liquid electrolytes, allowing better electrolyte retention, and our process relies on block-copolymer thermodynamics to create regular pore networks as opposed to non-equilibrium blending conditions.

Our two previous publications are limited in several regards. The first publication, presented in Chapter 2, outlines the effect of changing the length of the PS homopolymer relative to the PS block of the SES copolymer.[69] In our second publication, presented in Chapter 3,we utilize resonant soft x-ray scattering (RSoXS) to characterize the microphase separation processes occurring in our SES separators.[86] Each of these manuscripts utilizes a different block copolymer, but the relative size of the blocks in each copolymer is almost identical. In other words, we have been exploring only a single dimension of our parameter space – the relative

length of the PS homopolymer to PS block of the SES. In addition, we have not used many of the characterization methods directly relevant to battery manufacturing. In this manuscript, we study three different SES copolymers with identical PS-block lengths, but different PE block length. We find that the length of polyethylene chain has a strong effect on the pore structure and ionic conductivity (in liquid electrolyte) of the resulting SES separators. We take the optimal separators from each SES copolymer, perform tensile strength measurements on them, and cycle them in full coin cell batteries using graphite as the anode and $LiNi_{1/3}Co_{1/3}Mn_{1/3}O_2$ (NCM) as the cathode.

5.2 Experimental

Most of the characterization techniques used in this chapter are described in Chapter 1. The SES copolymer synthesis was modified in order to synthesize a series of SES copolymers with identical PS block length. Tensile strength experiments and battery cycling methods are also described here in this chapter.

Synthesis, characterization

The synthesis and characterization methods used in this study have been described in Chapter 1.[69] A series of three polystyrene-*block*-polybutadiene-*block*-polystyrene (SBS) copolymers were synthesized by sequential anionic polymerization with styrene and butadiene, followed by coupling of the resulting diblock copolymer.[8,9] To ensure that the PS block of the SBS copolymers was the same length for all three polymers, a single polystyrene was synthesized, and then divided into three equal portions using a pipette in an argon filled glove box. Butadiene was then added to each reaction vessel, and the diblock copolymers were coupled using dibromoethane. The C=C bonds in the polybutadiene block, with approximately 93% 1,4-addition, were saturated using *p*-toluenesulfonyl hydrazide in the presence of equimolar tri-*n*-propyl amine to give polystyrene-*block*-polyethylene-*block*-polystyrene (SES).[10] The molecular weights of individual blocks for the SES copolymers are listed in parentheses and are in units of kg mol^{-1}. For example, SES(13.5-67.2-13.5) represents a copolymer with PS, PE, and PS blocks with molecular weights of 13.5, 67.2, and 13.5 kg mol^{-1}, respectively.

Tensile Strength Measurements

Tensile strength measurements were performed using an electromechanical MTS Tytron 250 testing system equipped with a ± 25 N load cell. The SES films were cut into strips of approximately 5 mm x 50 mm, its final dimensions were measured with a ruler whereas film thicknesses were measured using a micrometer and ranged from 25 to 50 μm. The initial gauge length, x_0, varied between 20 and 30 mm. Films were stretched at a rate of 0.1 mm s^{-1} to a maximum axial displacement of 50 mm: the axial load, *F*, was recorded as a function of the axial displacement, Δx. The achieved tensile stress, S, is defined as $S = F/A_0$, where A_0 is the

initial cross sectional area of the film perpendicular to the loading direction, and the applied strain is $\varepsilon = \Delta x / x_0$. Subsequently, Young's modulus is calculated from the linear-elastic increase of the stress-strain curve by

$$E = \sigma / \varepsilon . \quad (8)$$

The yield stress, S_{YS} , is defined as the stress at which plastic deformation begins.

Battery Cycling

Coin cells were assembled in standard 2325 coin cell hardware purchased from National Research Council of Canada. Polypropylene separators (Celgard 2400) and SES separators were punched into circles with a diameter of 23.8 mm. $LiNi_{1/3}Co_{1/3}Mn_{1/3}O_2$ (NCM) was used as the active material in the positive electrode, and graphite (CGP-G8) was used as the active material in the negative electrode. The cells were crimped closed with a hydraulic crimping machine also manufactured by National Research Council of Canada. The entire procedure was performed in an argon-filled glove box. Cell testing was conducted on a Maccor Battery Cycler connected with a Thermotron Environmental Chamber set at 30ºC. Five formation cycles were performed at C/20 before the full cells were cycled between 3.0 and 4.3 V at C/2 for both charging and discharging rates.

The NCM powder used in the positive electrode was obtained from Umicore (Cellcore® MX-6). The graphite CGP-G8 used for the anode was purchased from Conoco Phillips. Battery-grade acetylene black (AB) with an average particle size of 40 nm and a material density of 1.95 g/cm^3 was acquired from Denka Singapore Private Limited. The binder polyvinylidene fluoride (PVDF 1100) was supplied by Kureha, Japan. Anhydrous N-methylpyrrolidone (NMP) was purchased from Aldrich Chemical Company. The 1.0 M lithium hexafluorophosphate ($LiPF_6$) in ethylene carbonate (EC): diethyl carbonate (DEC) (1:1 weight ratio) electrolyte was formulated by Novolyte Technologies.

The cathode mixture (92.8 wt% NCM, 3.2 wt% AB, and 4.0 wt% PVDF) was steadily dispersed in NMP using a Polytron PT10-35 homogenizer at 3000 rpm for 1 h. The slurry was then cast on a 20 μm thick battery-grade aluminum foil using a Mitutoyo doctor blade and a Yoshimitsu Seiki vacuum drawdown coater. After being dried overnight in an argon-filled glove box, the laminate was calendered to a porosity around 35% and then punched into 12.7 mm diameter discs. These punched electrodes were dried completely at 130°C in *vacuo* overnight before being assembled into coin cells. The CGP-G8 anode was prepared in the same way as the NMC cathode except that the solid mixture was composed with 89 wt% CGP-G8, 3.0 wt% AB, and 8.0 wt% PVDF, and the laminate was punched into 14.3 mm diam. discs.

Error analysis

The conductivity data reported are the average of at least 4-5 measurements. The tensile strength data reported represent the average of 4-5 measurements. The coin cell battery cycling data represent single cells: while multiple cells were measured, we present data from only 1 set.

5.3 Results and discussion

Samples

The samples discussed in this manuscript are summarized in Table 5. Three different block copolymers with identical PS block length (13.5 kg mol^{-1}) were synthesized. The PE block length ranged between 48 and 112 kg mol^{-1}. The molecular weight of the sacrificial homopolymer, $M_{n,sacrificial,PS}$, varied between 1.7 and 22.3 kg mol^{-1}. α is the ratio between sacrificial homopolymer PS and the S block of the SES copolymer, which means that α values are identical for all three SES copolymers tested. We fix the void fraction, ϕ_V, at 0.43 for all samples studied. The volume fraction of PE and PS in the porous separator, $\phi_{PE,BCP}$ and $\phi_{PS,BCP}$, are also presented.

Table 5. All samples studied in this chapter.

Sample	α	$M_{n,sacrificial,PS}$ (kg mol^{-1})	ϕ_V	$\phi_{PE,BCP}$	$\phi_{PS,BCP}$	E (MPa)*	S_{YS} (N mm^{-2})**
SES (13.5-112-13.5)	0.13	1.7	0.43	0.48	0.09		
SES (13.5-112-13.5)	0.22	3.0	0.43	0.48	0.09	41 ± 6	1.8 ± 0.2
SES (13.5-112-13.5)	0.36	4.8	0.43	0.48	0.09		
SES (13.5-112-13.5)	0.44	5.9	0.43	0.48	0.09		
SES (13.5-112-13.5)	0.90	12.2	0.43	0.48	0.09		
SES (13.5-112-13.5)	1.65	22.3	0.43	0.48	0.09		
SES (13.5-67-13.5)	0.13	1.7	0.43	0.43	0.14		
SES (13.5-67-13.5)	0.22	3.0	0.43	0.43	0.14		
SES (13.5-67-13.5)	0.36	4.8	0.43	0.43	0.14	94 ± 9	1.9 ± 0.1
SES (13.5-67-13.5)	0.44	5.9	0.43	0.43	0.14		
SES (13.5-67-13.5)	0.90	12.2	0.43	0.43	0.14		
SES (13.5-67-13.5)	1.65	22.3	0.43	0.43	0.14		
SES (13.5-48-13.5)	0.13	1.7	0.43	0.39	0.18		
SES (13.5-48-13.5)	0.22	3.0	0.43	0.39	0.18		
SES (13.5-48-13.5)	0.36	4.8	0.43	0.39	0.18		
SES (13.5-48-13.5)	0.44	5.9	0.43	0.39	0.18	109 ± 3	2.2 ± 0.3
SES (13.5-48-13.5)	0.90	12.2	0.43	0.39	0.18		
SES (13.5-48-13.5)	1.65	22.3	0.43	0.39	0.18		
Celgard 2400 (Machine Direction)						483 ± 39	49.8 ± 3.5
Celgard 2400 (Tensile Direction)						321 ± 37	13.4 ± 0.1

*Calculated using Equation 8.
**Calculated by determining elastic to plastic deformation point.

In Figure 23, we plot the ionic conductivity, σ, as a function of α for our SES separators in a liquid electrolyte (1 M $LiPF_6$ EC/DEC, 1:1, v/v). The conductivity of Celgard 2400, with ϕ_V = 0.41, in the same electrolyte (not plotted) is 0.42 mS cm^{-1}. For all three SES separators, σ is a strong function of α, where the conductivities are highest at intermediate α values (between 0.22 and 0.44) and drop precipitously at low (α = 0.13) and high ($\alpha \geq 0.90$) α values. These results are consistent with our previously published work. It is noteworthy that the optimal α value is different for each SES copolymer; yet the maximum conductivity is approximately the same (0.45 mS cm^{-1}). For the SES(13.5-48-13.5) separator, the conductivity peaks at σ = 0.45 mS cm^{-1} at α = 0.44. For the SES(13.5-67-13.5) separator, the conductivity plateaus at σ = 0.41 mS cm^{-1} between $0.22 \leq \alpha \leq 0.44$. Finally, for the SES(13.5-112-13.5) separator, the conductivity peaks at σ = 0.53 mS cm^{-1} at α = 0.22. We focus our benchmarking experiments on these three separators in the rest of the manuscript. In the case of the SES(13.5-67-13.5) separator, where σ plateaus across a range of α values, we use α = 0.37.

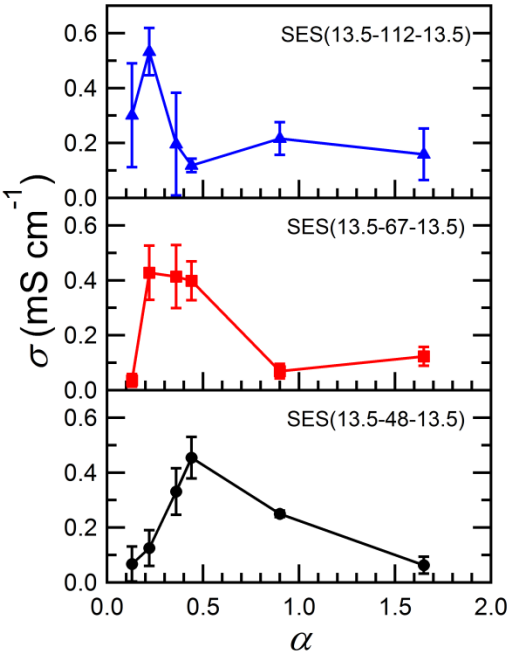

Figure 23. Ionic conductivity of all SES separators.
Ionic conductivity, σ, of SES separators soaked in 1.0 M $LiPF_6$ in EC/DEC 1:1 v/v as a function of the normalized chain length of the sacrificial homopolymer, α.

The optimal conductivity of our separators is not just a function of α; the molecular weight of the polyethylene block, M_{PE}, also has a strong effect on conductivity. In Figure 24, we plot σ as a function of M_{PE} for our block copolymers at α = 0.22 and α = 0.44. The conductivity data for these two α values show opposite dependences of σ on M_{PE}: for the α =

0.22 separators, σ increases with increasing M_{PE}, while for the α = 0.44 separators, σ decreases with increasing M_{PE}.

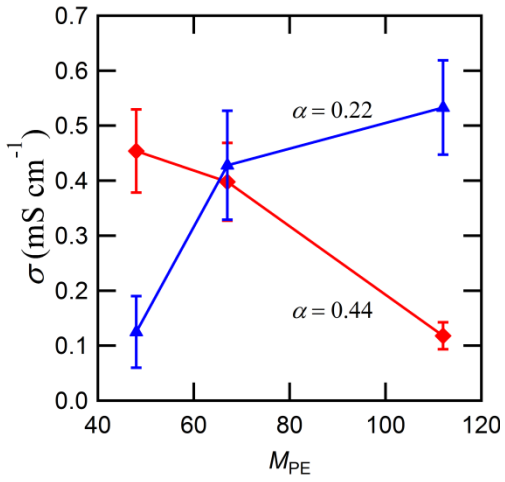

Figure 24. Ionic conductivity of SES separators at select α values as a function of M_{PE}.
Ionic conductivity, σ, of SES separators soaked in 1.0 M $LiPF_6$ in EC/DEC 1:1 v/v as a function of the molecular weight of the polyethylene block, M_{PE}, in the SES copolymers used.

In Figure 25a, b, and c, we show SEM images of the α = 0.44 separators for SES(13.5-48-13.5), SES(13.5-67-13.5), and SES(13.5-112-13.5), respectively. In Figure 25a and b, which represent the higher conductivity membranes, we see highly interconnected porous networks. However, in Figure 25c, we see large macro-sized pores throughout the membrane. These macropores are not well-connected throughout the film and therefore do no produce high conductivity separators. Macrophase separation has been seen before in our separators in Chapter 2,[69] but it occurred only when α was larger than 1; thus it is somewhat surprising to see this effect at such a low α value. In Figure 25a, d, and e, we show the benchmark samples described above: Figure 25a - SES(13.5-48-13.5), α = 0.44; Figure 25d - SES(13.5-67-13.5), α = 0.37; Figure 25e - SES(13.5-112-13.5), α = 0.22. All three of these membranes are similar in that they all have mesopores that permeate the entire structure, enabling high conductivities.

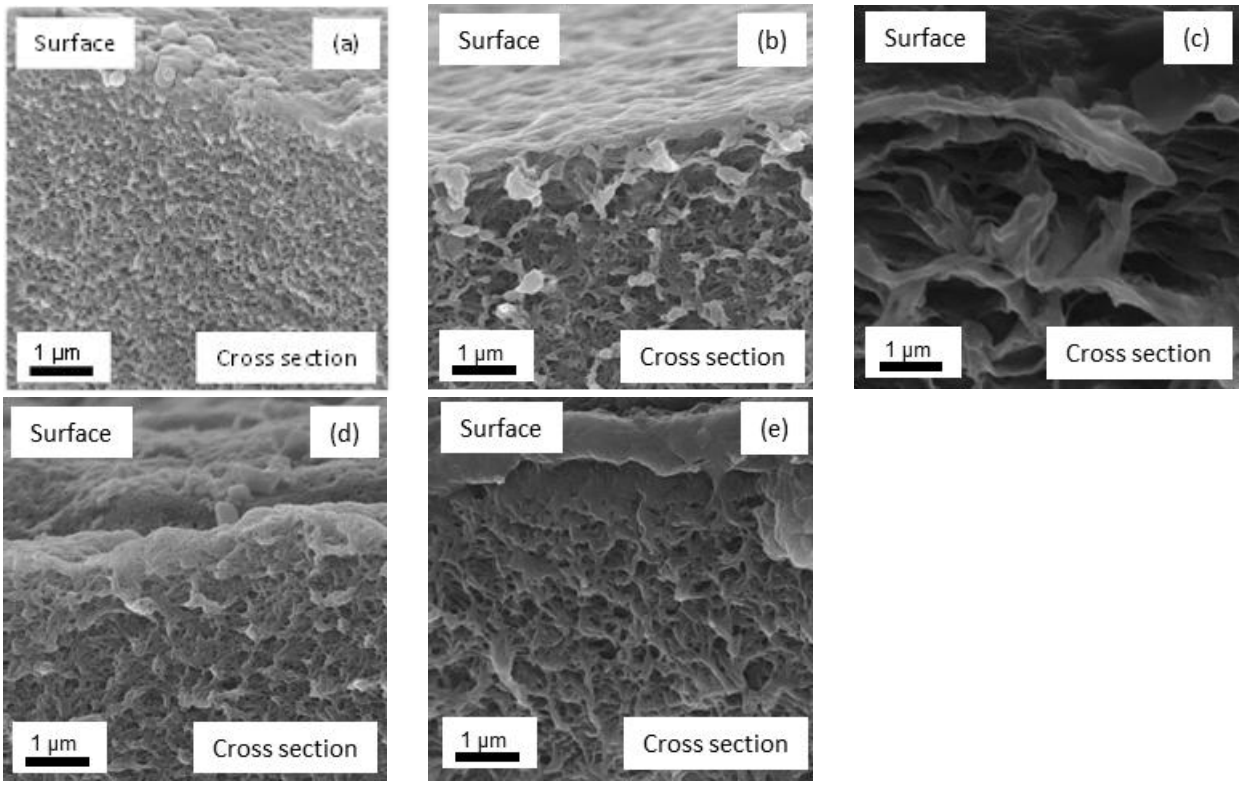

Figure 25. Scanning electron microscopy images of cross-section of SES separators.
(a) SES (13.5-48-13.5), α = 0.44 (b) SES (13.5-67-13.5), α = 0.44 (c) SES (13.5-112-13.5), α = 0.44 (d) SES (13.5-67-13.5), α = 0.37 (e) SES (13.5-112-13.5), α = 0.22.

Figure 26 shows stress, S, as a function of strain, ε, for benchmark SES separators and for Celgard 2400. We can see that there is a significant difference in the stress that the SES separators (Figure 26a-c) can withstand compared to the Celgard (Figure 26d). Young's modulus, E, was calculated using Equation 8 by fitting a line to the linear-elastic increase of the $S-\varepsilon$ curve (ε < 0.05). The yield stress, S_{YS}, is the stress at which the films transition from elastic to plastic deformation. In Table 5, we tabulate measured values of E and S_{YS} for our benchmark SES separators and Celgard 2400. Celgard 2400 data are separated into the machine direction (MD), and the tensile direction (TD), which are a result of the stretching processes used to make the pore structure in the Celgard separators. In the context of this manuscript, the distinction between MD and TD is important only in the respect that they are the upper and lower limits for the tensile properties of Celgard 2400. We note that because our separators films are cast, without any in-plane orientation steps, our films do not display differences in tensile properties as a result of the direction of strain, ie. no MD and TD directions.

The tensile properties of battery separators are important for both roll-to-roll manufacturing and in resisting deformation during battery cycling. We see that our SES separators have a significantly lower E and S_{YS} than our Celgard benchmark. This is not surprising as our SES separators have not undergone the mechanical property optimizations used in commercial battery separators and polymers. For our SES separators, S_{YS} seems to be only a weak function of M_{PE}, while E is a strong function of M_{PE}: the shorter chain SES(13.5-48-13.5)

separators have the highest E. This increase in Young's Modulus is the result of the triblock copolymer morphology. The lower molecular weight PE-blocks of the SES allows for the presence of more short, strong bridges across the domains.[6]

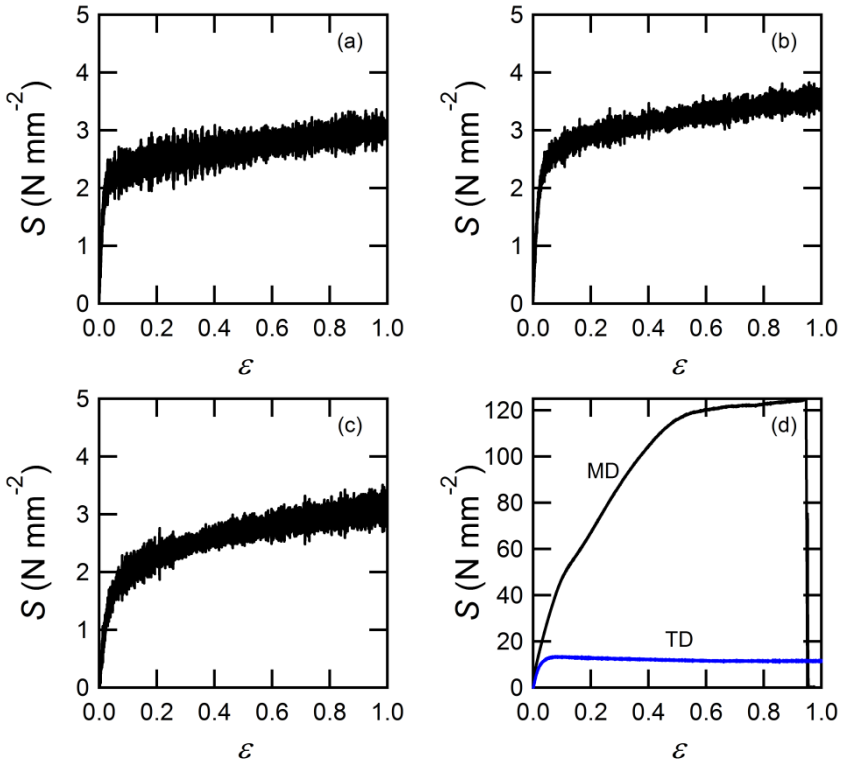

Figure 26. Stress-strain curves for SES separators and Celgard.
Stress, S, as a function of strain, ε, for (a) SES (13.5-48-13.5), α = 0.44, (b) SES (13.5-67-13.5), α = 0.37, (c) SES (13.5-112-13.5), α = 0.22, (d) Celgard 2400.

In Figure 27 we plot discharge capacity (black diamonds) and Coulombic efficiency (orange triangles) for the first 100 C/2 cycles for our benchmark SES separators and for Celgard 2400. The discharge capacities are normalized for the mass of NCM cathode material used, which has a specific capacity of approximately 140 mAh/g. For the SES(13.5-48-13.5) separator in Figure 27a and the SES(13.5-67-13.5) separator in Figure 27b, we see very similar behavior: the discharge capacity rapidly decreases over the first 20 cycles from approximately 120 to 100 mAh g^{-1}, before gradually decreasing over the remaining 80 cycles. By contrast, the SES(13.5-112-13.5) separator in Figure 27c shows very unusual behavior, in that the capacity decreases rapidly over the first 40 cycles from 138 to 100 mAh g^{-1}, before recovering slightly and leveling off. In Figure 27d, we show the discharge curve for our benchmark Celgard 2400 separator, where the discharge capacity decreased gradually from 133 to 128 mAh g^{-1} over 100 cycles. The discharge curves are not ideal for any of the SES separators shown, particularly SES(13.5-112-13.5) (Figure 27c). The initial irrecoverable and rapid decrease in capacity over the first 20 cycles suggests the occurrence of parasitic reactions. Still, it is encouraging that the Coulombic efficiency levels off to approximately 1.0 after the first few cycles.

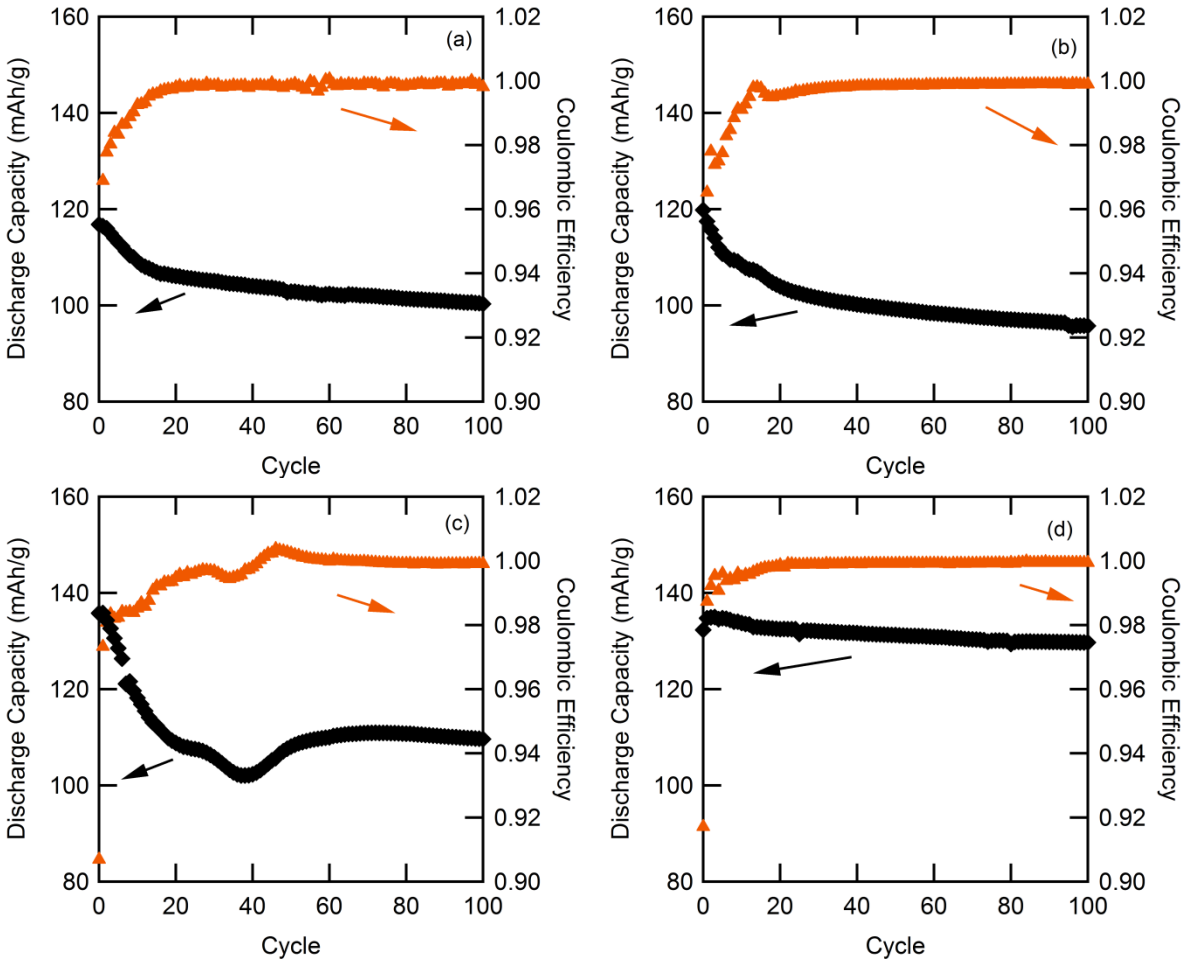

Figure 27. **Discharge curves for full cell batteries using SES separators and Celgard.** Discharge capacity (left) and Coulombic Efficiency (right) as a function of cycle number for (a) SES (13.5-48-13.5), α = 0.44, (b) SES (13.5-67-13.5), α = 0.37, (c) SES (13.5-112-13.5), α = 0.22, (d) Celgard 2400. Coin cells were cycled at C/20 5 times (formation cycles) and then cycled at C/2.

The primary two purposes of this manuscript are to demonstrate the effect of M_{PE} on the conductivity of our block copolymer battery separators and to benchmark these SES separators against a commercial separator. We see that while the optimal value of α is different for the each SES, the peak σ is approximately the same. These conductivities are similar to Celgard (in the same electrolyte) with approximately the same void fraction. This means that our strategy for synthesizing these mesoporous separators can potentially be applied to a wide molecular weight range of block copolymers without a significant decrease in conductivity. We also see that by decreasing M_{PE}, the modulus (see Figure 26 and Table 5) can be increased significantly. While the tensile properties of our SES separators do not compare favorably with Celgard, we note that different processing techniques and using a less-branched PE (recall that our synthetic strategy gives only 93% unbranched PE) could dramatically increase both the modulus and yield stress. The exact cause for the initial decrease in discharge capacity in our batteries is not entirely clear.

However, the performance seems to level off quickly, and we see that the lower molecular weight SES separators outperform the higher molecular weight separators.

5.4 Conclusions

A series of mesoporous block copolymer battery separators was synthesized and benchmarked against Celgard 2400, a commercial battery separator. The block copolymer separators were synthesized using a strategy analogous to the wet process used in commercial battery separators; polystyrene-*block*-polyethylene-*block*-polystyrene (SES) copolymers were made porous with the use of a sacrificial polystyrene (PS) homopolymer. Three SES copolymers were synthesized with an identical PS-block molecular weight of 13.5 kg mol^{-1}, and a PE block molecular weight, M_{PE}, ranging from 48 to 112 kg mol^{-1}. The molecular weight of the optimal sacrificial PS homopolymer varied greatly with M_{PE}, but the maximum conductivities measured were approximately the same, regardless of M_{PE}. The Young's modulus measured from tensile strength experiments was a strong function of M_{PE}, and increased with decreasing M_{PE}. Full cell batteries were cycled, and the cycling data were more consistent in the low M_{PE} separators. In both tensile strength experiments and battery cycling, SES separators did not compare favorably with Celgard, but showed clear directions for improvement.

References

1. Ihm, D.; Noh, J.; Kim, J. *Journal of Power Sources* **2002,** 109, (2), 388-393.
2. Weighall, M. J. *Journal of Power Sources* **1991,** 34, (3), 257-268.
3. Zhang, S. S. *Journal of Power Sources* **2007,** 164, (1), 351-364.
4. Gaines, L. C., R., Costs of Lithium-Ion Batteries for Vehicles. In Energy, D. o., Ed. Argonne, Illinois, 2000.
5. Nasef, M. M.; Saidi, H. *Macromolecular Materials and Engineering* **2006,** 291, (8), 972-983.
6. Drolet, F.; Fredrickson, G. H. *Macromolecules* **2001,** 34, (15), 5317-5324.
7. Matsen, M.; Thompson, R. *The Journal of chemical physics* **1999,** 111, 7139.
8. Morton, M.; Fetters, L. J. *Rubber Chem. Technol.* **1975,** 48, 359.
9. Lin, Y. C.; Tsiang, R. C. C. *Journal of Applied Polymer Science* **1997,** 64, (13), 2543-2560.
10. Hahn, S. F. *Journal of Polymer Science Part a-Polymer Chemistry* **1992,** 30, (3), 397-408.
11. Mark, J. E.; Eitouni, H. B.; Balsara, N. P., Thermodynamics of Polymer Blends. In *Physical Properties of Polymers Handbook*, Springer New York: 2007; pp 339-356.
12. Brandrup, J.; Immergut, E. H., *Polymer Handbook*. Third ed.; John Wiley & Sons: New York, 1989.
13. Brunauer, S.; Emmett, P. H.; Teller, E. *Journal of the American Chemical Society* **1938,** 60, 309-319.
14. Sing, K. S. W.; Everett, D. H.; Haul, R. A. W.; Moscou, L.; Pierotti, R. A.; Rouquerol, J.; Siemieniewska, T. *Pure and Applied Chemistry* **1985,** 57, (4), 603-619.
15. Ilavsky, J. *Journal of Applied Crystallography* **2012,** 45, 324-328.
16. Gann, E.; Young, A. T.; Collins, B. A.; Yan, H.; Nasiatka, J.; Padmore, H. A.; Ade, H.; Hexemer, A.; Wang, C. *Review of Scientific Instruments* **2012,** 83, (4).
17. Balsara, N. P. *Current Opinion in Solid State & Materials Science* **1998,** 3, (6), 589-595.
18. Datta, S.; Lohse, D. J. *Macromolecules* **1993,** 26, (8), 2064-2076.
19. Jeon, H. S.; Lee, J. H.; Balsara, N. P. *Macromolecules* **1998,** 31, (10), 3328-3339.
20. Lefebvre, A. A.; Lee, J. H.; Jeon, H. S.; Balsara, N. P.; Hammouda, B. *Journal of Chemical Physics* **1999,** 111, (13), 6082-6099.
21. Lohse, D. J. *Polymer Engineering and Science* **1986,** 26, (21), 1500-1509.
22. De Gennes, P. G. *Journal of Chemical Physics* **1971,** 55, (2), 572-579.
23. Ferry, J. D., *Viscoelastic Properties of Polymers*. 3rd Edition ed.; John Wiley & Sons: 1980.
24. Graessley, W. W., *Polymeric Liquids & Networks: Dynamics and Rheology*. Taylor & Francis Group, LLC: London, 2008; p 801.
25. Flory, P. I. *Journal of Chemical Physics* **1942,** 10, (1), 51-61.
26. Huggins, M. L. *Journal of Physical Chemistry* **1942,** 46, (1), 151-158.
27. Lynd, N. A.; Hillmyer, M. A. *Macromolecules* **2005,** 38, (21), 8803-8810.
28. Pitet, L. M.; Amendt, M. A.; Hillmyer, M. A. *Journal of the American Chemical Society* **2010,** 132, (24), 8230-8231.
29. Ruzette, A. V.; Tence-Girault, S.; Leibler, L.; Chauvin, F.; Bertin, D.; Guerret, O.; Gerard, P. *Macromolecules* **2006,** 39, (17), 5804-5814.
30. Widin, J. M.; Schmitt, A. K.; Im, K.; Schmitt, A. L.; Mahanthappa, M. K. *Macromolecules* **2010,** 43, (19), 7913-7915.

31. Bates, F. S.; Fredrickson, G. H. *Annual Review of Physical Chemistry* **1990,** 41, 525-557.
32. Leibler, L. *Macromolecules* **1980,** 13, (6), 1602-1617.
33. Matsen, M. W.; Bates, F. S. *Macromolecules* **1996,** 29, (4), 1091-1098.
34. Loo, Y. L.; Register, R. A.; Ryan, A. J. *Physical Review Letters* **2000,** 84, (18), 4120-4123.
35. Loo, Y. L.; Register, R. A.; Ryan, A. J. *Macromolecules* **2002,** 35, (6), 2365-2374.
36. Loo, Y. L.; Register, R. A.; Ryan, A. J.; Dee, G. T. *Macromolecules* **2001,** 34, (26), 8968-8977.
37. Quiram, D. J.; Register, R. A.; Marchand, G. R. *Macromolecules* **1997,** 30, (16), 4551-4558.
38. Hamley, I. W.; Fairclough, J. P. A.; Bates, F. S.; Ryan, A. J. *Polymer* **1998,** 39, (6-7), 1429-1437.
39. Hamley, I. W.; Fairclough, J. P. A.; Terrill, N. J.; Ryan, A. J.; Lipic, P. M.; Bates, F. S.; TownsAndrews, E. *Macromolecules* **1996,** 29, (27), 8835-8843.
40. Ryan, A. J.; Hamley, I. W.; Bras, W.; Bates, F. S. *Macromolecules* **1995,** 28, (11), 3860-3868.
41. Schmalz, H.; Knoll, A.; Muller, A. J.; Abetz, V. *Macromolecules* **2002,** 35, (27), 10004-10013.
42. Caze, C.; Pak, S. H. *Journal of Materials Science Letters* **1997,** 16, (1), 53-55.
43. Wu, S. *Journal of Physical Chemistry* **1970,** 74, (3), 632-638.
44. Phillip, W. A.; Rzayev, J.; Hillmyer, M. A.; Cussler, E. L. *Journal of Membrane Science* **2006,** 286, (1-2), 144-152.
45. Uehara, H.; Kakiage, M.; Sekiya, M.; Sakuma, D.; Yamonobe, T.; Takano, N.; Barraud, A.; Meurville, E.; Ryser, P. *Acs Nano* **2009,** 3, (4), 924-932.
46. Yang, S. Y.; Ryu, I.; Kim, H. Y.; Kim, J. K.; Jang, S. K.; Russell, T. P. *Advanced Materials* **2006,** 18, (6), 709-712.
47. Yang, S. Y.; Yang, J. A.; Kim, E. S.; Jeon, G.; Oh, E. J.; Choi, K. Y.; Hahn, S. K.; Kim, J. K. *Acs Nano* **2010,** 4, (7), 3817-3822.
48. Zhou, N.; Bates, F. S.; Lodge, T. P. *Nano Letters* **2006,** 6, (10), 2354-2357.
49. Shull, K. R. *Journal of Chemical Physics* **1991,** 94, (8), 5723-5738.
50. Leibler, L. *Makromolekulare Chemie-Macromolecular Symposia* **1988,** 16, 1-17.
51. Feng, X.; Fryxell, G. E.; Wang, L. Q.; Kim, A. Y.; Liu, J.; Kemner, K. M. *Science* **1997,** 276, (5314), 923-926.
52. Hoffmann, F.; Cornelius, M.; Morell, J.; Froba, M. *Angewandte Chemie-International Edition* **2006,** 45, (20), 3216-3251.
53. Jeong, U. Y.; Ryu, D. Y.; Kim, J. K.; Kim, D. H.; Russell, T. P.; Hawker, C. J. *Advanced Materials* **2003,** 15, (15), 1247-1250.
54. Liu, G. J.; Ding, J. F.; Guo, A.; Herfort, M.; BazettJones, D. *Macromolecules* **1997,** 30, (6), 1851-1853.
55. Rzayev, J.; Hillmyer, M. A. *Macromolecules* **2005,** 38, (1), 3-5.
56. Rzayev, J.; Hillmyer, M. A. *Journal of the American Chemical Society* **2005,** 127, (38), 13373-13379.
57. Hashimot.T; Nagatosh.K; Todo, A.; Hasegawa, H.; Kawai, H. *Macromolecules* **1974,** 7, (3), 364-373.
58. Hashimoto, T.; Todo, A.; Itoi, H.; Kawai, H. *Macromolecules* **1977,** 10, (2), 377-384.

59. Hadziioannou, G.; Picot, C.; Skoulios, A.; Ionescu, M. L.; Mathis, A.; Duplessix, R.; Gallot, Y.; Lingelser, J. P. *Macromolecules* **1982,** 15, (2), 263-267.
60. Richards, R. W.; Thomason, J. L. *Polymer* **1981,** 22, (5), 581-589.
61. Bates, F. S.; Fetters, L. J.; Wignall, G. D. *Macromolecules* **1988,** 21, (4), 1086-1094.
62. Graessley, W. W.; Krishnamoorti, R.; Balsara, N. P.; Fetters, L. J.; Lohse, D. J.; Schulz, D. N.; Sissano, J. A. *Macromolecules* **1994,** 27, (9), 2574-2579.
63. Mitchell, G. E.; Landes, B. G.; Lyons, J.; Kern, B. J.; Devon, M. J.; Koprinarov, I.; Gullikson, E. M.; Kortright, J. B. *Applied Physics Letters* **2006,** 89, (4).
64. Virgili, J. M.; Tao, Y. F.; Kortright, J. B.; Balsara, N. P.; Segalman, R. A. *Macromolecules* **2007,** 40, (6), 2092-2099.
65. Swaraj, S.; Wang, C.; Araki, T.; Mitchell, G.; Liu, L.; Gaynor, S.; Deshmukh, B.; Yan, H.; McNeill, C. R.; Ade, H. *European Physical Journal-Special Topics* **2009,** 167, 121-126.
66. Swaraj, S.; Wang, C.; Yan, H. P.; Watts, B.; Jan, L. N.; McNeill, C. R.; Ade, H. *Nano Letters* **2010,** 10, (8), 2863-2869.
67. Wang, C.; Lee, D. H.; Hexemer, A.; Kim, M. I.; Zhao, W.; Hasegawa, H.; Ade, H.; Russell, T. P. *Nano Letters* **2011,** 11, (9), 3906-3911.
68. Yan, H. P.; Collins, B. A.; Gann, E.; Wang, C.; Ade, H.; McNeill, C. R. *Acs Nano* **2012,** 6, (1), 677-688.
69. Wong, D. T.; Mullin, S. A.; Battaglia, V. S.; Balsara, N. P. *Journal of Membrane Science* **2012,** 394, 175-183.
70. Eitouni, H. B.; Balsara, N. P.; Mark, J. E., Thermodynamics of Polymer Blends Physical Properties of Polymers Handbook. In Springer New York: 2007; pp 339-356.
71. Mansour, A. S.; Johnson, L. F.; Lodge, T. P.; Bates, F. S. *Journal of Polymer Science Part B-Polymer Physics* **2010,** 48, (5), 566-574.
72. We were unable to find a listing of $\chi_{PE/PS}$. However, we were able to find chi between polyvinylcyclohexane and PE in ref [31], and this is the value we use in our analysis. Similar values have been obtained for χ between PS and other saturated polyolefins.[70]
73. Lorenzo, A. T.; Arnal, M. L.; Muller, A. J.; Boschetti-de-Fierro, A.; Abetz, V. *Macromolecules* **2007,** 40, (14), 5023-5037.
74. Hamley, I. W.; Castelletto, V. *Progress in Polymer Science* **2004,** 29, (9), 909-948.
75. Loo, Y. L.; Register, R. A.; Adamson, D. H. *Macromolecules* **2000,** 33, (22), 8361-8366.
76. Register, R. A.; Rangarajan, P.; Quiram, D. J.; Loo, Y. L.; Marchand, G. R.; Fetters, L. J. *Abstracts of Papers of the American Chemical Society* **2000,** 219, U474-U474.
77. Likhtman, A. E.; Semenov, A. N. *Macromolecules* **1997,** 30, (23), 7273-7278.
78. Matsen, M. W. *Macromolecules* **1995,** 28, (17), 5765-5773.
79. Matsen, M. W. *Macromolecules* **2003,** 36, (25), 9647-9657.
80. Tanaka, H.; Hasegawa, H.; Hashimoto, T. *Macromolecules* **1991,** 24, (1), 240-251.
81. Roe, R.-J., *Methods of X-ray and neutron scattering in polymer science*. Oxford Univ. Press: New York, NY [u.a.], 2000.
82. Strobl, G. R., *The physics of polymers: concepts for understanding their structures and behavior*. Springer Verlag: 1997.
83. Dhez, O.; Ade, H.; Urquhart, S. G. *Journal of Electron Spectroscopy and Related Phenomena* **2003,** 128, (1), 85-96.
84. Muller, A. J.; Balsamo, V.; Arnal, M. L. *Block Copolymers Ii* **2005,** 190, 1-63.
85. Rangarajan, P.; Register, R. A.; Fetters, L. J. *Macromolecules* **1993,** 26, (17), 4640-4645.

86. Wong, D. T.; Wang, C.; Beers, K. M.; Kortright, J. B.; Balsara, N. P. *Macromolecules* **2012**.
87. Zhang, F.; Ilavsky, J.; Long, G. G.; Quintana, J. P. G.; Allen, A. J.; Jemian, P. R. *Metallurgical and Materials Transactions a-Physical Metallurgy and Materials Science* **2010,** 41A, (5), 1151-1158.
88. Wignall, G. D.; Bates, F. S. *Journal of Applied Crystallography* **1987,** 20, 28-40.
89. Glinka, C. J.; Barker, J. G.; Hammouda, B.; Krueger, S.; Moyer, J. J.; Orts, W. J. *Journal of Applied Crystallography* **1998,** 31, 430-445.
90. Mark, J. E., *Physical properties of polymers handbook*. Springer: 2006.